Investigating Br···(HCCH)$_n$, Cl···(HCCH)$_n$ and I···(HCCH)$_n$ using Anion Photoelectron Spectroscopy and *ab initio* Calculations

---

Shanee Conran

Summary

Anion photoelectron spectroscopy is a method of exploring solvent-solute and solvent-solvent interactions in the gas-phase. The spectra taken using a Time of Flight Mass Spectrometer coupled with a Time of Flight Photoelectron Spectrometer can be combined with *ab initio* calculations to gain a deeper understanding of the solvation phenomenon.

Clusters of acetylene with central atoms of chloride, bromide and iodide have been explored. Mass spectra of all three complexes were able to be taken with multiple clusters of the halide-acetylene complexes being seen.

Both the anion and neutral species were investigated using *ab initio* calculations. The optimised structures of the anion complexes were confirmed to be linear with a strong interaction evident in the changing of bond lengths, vibrational frequencies and movement of electron density. A decrease in the strength of the interaction was also observed with an increasing halide size.

The neutral species have two optimised geometries: linear and a T-shape where the halogen is located above the carbon triple bond. The T-shape neutral geometry is the more stable geometry. These structures were similarly analysed as the anion species. Similar to the anion, there is also a decrease in interaction strength due to increasing halogen size. Due to the lack of a charge on the halogen there is an overall decrease in the strength of the interaction between the central halogen and the acetylene.

Declaration

This paper contains no material which has been accepted for the award of any other degree or diploma in any university.

To the best of my knowledge, this paper contains no material previously published or written by any other person except where due reference or acknowledgement is made.

Shanee Conran

29 November 2013

Acknowledgements

I first have to thank Duncan Wild for being an amazing supervisor. Thank you for all of your help and putting up with my general incompetence with good humour and patience. And also thank you for putting up with my 'magnetic personality' that had the machine see so much down time this year.

I'd like to thank Kim Lapere for all her help and guidance. Thank you for showing me the ropes and saving the day on multiple occasions. I have greatly appreciated all your general know-how and wisdom, support and friendship this year.

Thank you to the other members of the Wild Lab: Marcus Kettner, Chia-yang Lim, Richard Bentley-Moyse and Duncan Beckham. Thank you all for putting up with me this year. I've had lots of fun!

I also need to thank the members of the workshop: Nigel Hamilton, Andrew Sawyer, Damien Bainbridge and Trevor Franklin for dedicatedly working on the TOF-PES and getting it to where it is today.

And finally thank you to my friends and family who have tolerated my bad moods and stress and offered their support. This year would not have been possible without you.

Table of Contents

1 Introduction

The solvation phenomenon between neutral ligands and anion cores can be explored by analysing gas-phase negatively-charged clusters. This can lead to information about the solvent-solvent and solute-solvent interactions, the hydrogen bonding and the distribution of electron density. Time of flight mass spectroscopy is a suitable technique to use because it enables the examination of the step-wise addition of ligands into the solvation shell of the anion. By using photoelectron spectroscopy, a greater understanding of the solvation phenomenon at a microscopic level can be reached and then applied to a bulk-context.

1.1 Project aims

In this project, the solvation phenomenon has been explored by looking at the addition of acetylene ligands around a central anion being chloride, bromide and iodide. This has been done by generating clusters of $X^{-}\cdots(HCCH)_n$ (X=Cl, Br, I) and analysing them using anion photoelectron spectroscopy. The Time of Flight Mass Spectrometer (TOF-MS) in the Wild lab is capable of looking at the step-wise addition of the ligands by separating ion clusters by mass. These clusters can then be individually analysed through photoelectron spectroscopy and compared to one another.

In addition, *ab initio* calculations have been carried out on the neutral and anion states of chloride-acetylene, bromide-acetylene and iodide-acetylene in a 1:1 ratio in order to gain complementary theoretical data to that observed using photoelectron spectrometry.

This work leads on from the previous work by Wild *et al.* on $Cl^{-}\cdots(HCCH)_n$, $Br^{-}\cdots(HCCH)_n$ and $I^{-}\cdots(HCCH)_n$ using Time of Flight Photoelectron Spectroscopy to extend the number of ligands detected around the central anion and further deduce information about the solvation phenomenon.

1.2 Solvation

Understanding and being able to predict and explain the behaviour of ions in a solution is only possible with an understanding of the interactions between the ion and the solvent molecules. Solvation occurs in both the condensed and gas phases and is a fundamental part of understanding chemistry and the ways reactions proceed.

An example of fundamental understanding would be the low reactivity of fluoride in aqueous solution. This is due to the strong binding of water molecules to the fluoride via solvation. In comparison, fluoride in the gas phase shows a high reactivity. Solvation plays an important role in the stability of small charged anions, that are unstable without any solvent molecules surrounding them.[1]

A good way to look at solvation is by using gas-phase spectroscopy. This technique is capable of obtaining direct empirical information about the structure of these clusters. Studies into gas-phase spectroscopy have been occurring since the 1960's and have been concerned with looking at charged complexes of neutral molecules attached to central ions.[1]

The solvation clustering equilibrium can be seen in equation 1:

$$A^{\pm m} - L_n + L \rightleftharpoons A^{\pm m} - L_{(n+1)} \qquad \textbf{(1)}$$

where A is the central ion and L is the solvent molecule or atom that surrounds A.[2]

1.2.1 Ion-molecule complex clusters

Ion-molecule complex cluster spectroscopy is concerned with studying the solvation phenomenon on a microscopic level, i.e. modelling ion-solvent interactions. The understanding of these interactions is important for structural and energetic properties of electrolyte solutions.[1]

By studying the solvation phenomenon at a microscopic scale the results can then be transferred to a bulk context. The exploration of a number of different ligands examines the effects that the strength of the solvent-solute interactions can have on the solvation phenomenon. The differences in how the clusters are made up can result in large differences in the geometry or the dynamics which would then be carried over to what is seen in the bulk context.[3]

The structure of the cluster depends on the strength and nature of the solvent-solvent interactions and the competition with the solvent-solute interactions.[1] By looking at a variety of ligands around ions, we increase our understanding of the nature of solvation and of clustering.

1.2.2 Hydrogen bonding in halide-clusters

By examining the step-wise addition of ligands around a central atom, inferences can be made about the structure of the cluster. This can then lead to information about competing solvent-solvent and solvent-atom interactions. Due to the small size of the ligands and the relatively large size of the halide ions, larger clusters of ligands around the halide can form, making halides good candidates for exploring the solvation phenomenon.[4]

Due to the large electronegativities of fluorine and chlorine, they can form hydrogen bonds with hydrogen-containing ligands. Bromine and iodine, due to their weaker proton acceptor abilities are seen to form the weaker van der Waals interactions with ligands. However in the anion state, all the halide anions form very strong hydrogen bond interactions.[4] The hydrogen bonding helps determine the structure of the complex, based on the distribution of the electron density around the hydrogen and the proton acceptor. This phenomenon has been observed in both the solid and gas phases

1.3 The Photoelectric Effect

Einstein's photoelectric effect describes the interaction of an incoming photon with an atom or molecule. The photoelectric effect states that if the incoming photon has sufficient energy, it will overcome the electron's binding energy and it will eject from the electron shell with a known kinetic energy according to equation 2:

$$KE = hv - BE \qquad \textbf{(2)}$$

where KE is kinetic energy of the ejected electron, *hv* is the energy of the incoming photon and BE is the binding energy of the electron.

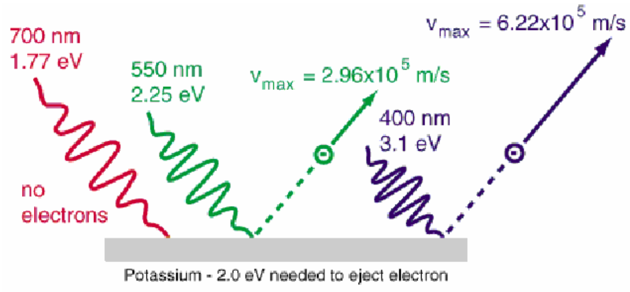

Figure 1. Diagram of the photoelectric effect[5]

In Figure 1, photons of different wavelengths interact with potassium, which requires 2.0 eV to eject an electron. The red wavelength corresponds to 1.77 eV and is unable to overcome the binding energy of potassium. The green and blue wavelengths correspond to both greater than 2.0 eV and so electrons are ejected. Because of the different initial energy of the blue and green wavelengths, the electrons are ejected from the potassium with different kinetic energies.

In Photoelectron spectroscopy, the energy of the incoming photon is known and constant throughout the clusters being analysed. The kinetic energy of the photoelectron is measured by the photoelectron spectrometer. By looking at the kinetic energy, the binding energy of the photoelectron can be calculated and inferences about its properties and the cluster from which it came can be made.

1.3.1 Potential Energy Surfaces

Potential energy surfaces are a graphical representation of a reaction process. They are created by mapping the changes to the energy of the system through variations of different features in the structure such as bond lengths and angles.[6,7]

The most stable state of the geometry can be determined by the global minimum on a potential energy surface. Other minima on the potential energy surface are intermediate states in the reaction. Maxima represent transition states. For clusters that can have multiple structures and bonding formations with the ligands, potential energy surfaces are important for determining the most stable structure and understanding the interactions between the solvent and ion.

In the analysis of $X^{-}\cdots(HCCH)_n$ (X=Cl, Br, I) clusters using photoelectron spectroscopy the potential energy surfaces of the neutral complexes can be determined. Upon interaction with the laser, the anion cluster is excited into the neutral state. The most likely transition into the neutral state occurs where there is the best overlap of the vibrational energy levels' wavefunctions. When the complex then transitions to a lower vibrational state of the neutral complex, a photoelectron of a particular energy is ejected (Figure 2).

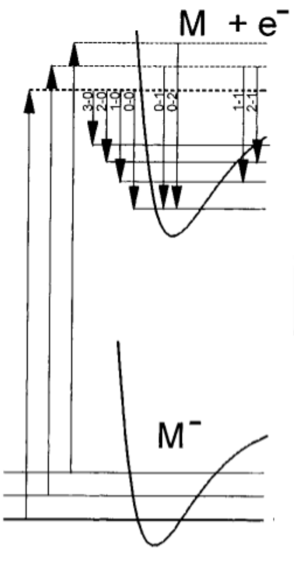

Figure 2. Diagram showing the transition from the anion potential surface to the neutral potential surface upon interaction with a light source[5]

Because of this, the information of the photoelectron gathered by photoelectron spectroscopy refers to the neutral potential energy surface. The anion-neutral transition is used because of the stability of the anion clusters and the accessibility of more vibrational electronic neutral states. This is due to favourable geometry changes or different selection rules compared to the neutral-neutral transition.[8]

1.4 Past Research

A number of studies have been done on the nature of hydrogen bonds in solvent-solute interactions between halides and various ligands. These multiple studies of different ligands around the same group of central atoms lead to some comparison between the results for changes in the structure determination and spectra as the strength of the competing interactions changes.

In weaker ligands such as carbon monoxide[9] the ligands form a solvation shell around the central halide. The solvent-solvent interactions force the ligands into sterically favourable positions around the ion, i.e. they are evenly spaced around the central halide. This structure is in contrast to complexes where the solvent-solute interactions are of a similar strength to the solvent-solvent interactions, such as in halide-water clusters. Instead of forming a solvation shell, the water ligands form a network by bonding to each other and the halide bonds to the top of the water network.[10] It is only in fluoride-water clusters that the strong, favoured fluoride-hydrogen bond forces the creation of a solvation shell as seen with weaker ligands.[4,11]

For non-linear ligands such as H_2O, NH_3 and NH_4, it has been seen that in some structures the hydrogens in these ligands can form multiple hydrogen bonds with the same central ion. However, with these multiple structures, it has been found that the monodentate structure (with only one hydrogen bond to the central ion) is the global minimum on the potential energy curve. Other structures are transition states or less favoured.[4]

Spectra by Arnold *et al.*[3] show comparisons between clusters of two different ligands, and clusters that have the same ligand but a different central halide. By comparing $I^- \cdots (N_2O)_n$ and $I^- \cdots (CO_2)_n$ the differences in the strength of the solvent-solute interactions and the solvent-solvent interactions can be seen through the structure of the clusters and their spectra. The stronger $I^- \cdots (CO_2)_n$ interaction results in a distortion of the ligand and a smaller solvation shell around the ion as the ligands bind closer and more strongly.

Also by Arnold *et al.*[3] is a comparison between $I^- \cdots (CO_2)_n$ and $Br^- \cdots (CO_2)_n$. In these spectra a difference in the ion-ligand strength is seen by looking at the step-wise addition of ligands around the central halide. While their spectra both look very similar there is suggestion of a smaller first solvation shell around the bromide as well as a stronger binding energy in comparison to the iodide.

Acetylene has weak solvent-solvent interactions in comparison to water ligands. In addition, the ligands have a linear structure which would prevent one of the ligands from forming hydrogen bonds with neighbouring acetylenes that are also bonded to the halide core. Thus it is expected to produce a simpler structure than a water complex. The acetylene ligands should surround the halide core in the solvation shell as seen in other weaker solvent-solvent interaction ligands.[10]

1.4.1 Chloride-acetylene anion clusters

Chloride-acetylene clusters have been studied previously using both experimental methodology and *ab initio* calculations. The experimental work has been carried out by Wild *et al.*[12] using IR spectroscopy to look at the step-wise addition of ligands in the $Cl^- \cdots (HCCH)_n$ complex where n=1-9. This study found the structure of the complex from n=1-6 to be evenly spaced acetylene ligands around the central ion due to the weak acetylene-acetylene interactions (Figure 3).

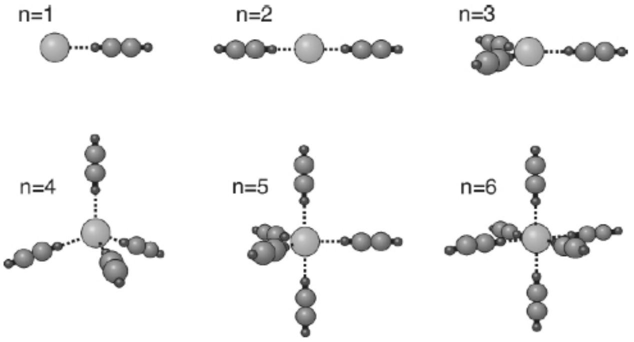

Figure 3. n=1-6 structures of $Cl^{-}\cdots(HCCH)_n$ complex[12]

The spectra of the first n=1-6 ligands showed a single major peak indicating the presence of a single geometry. The step-wise addition of the ligands caused a shift in the signal of the cluster closer to the wavelength of a free acetylene showing a decrease in the chloride-acetylene interaction as each additional ligand was added.

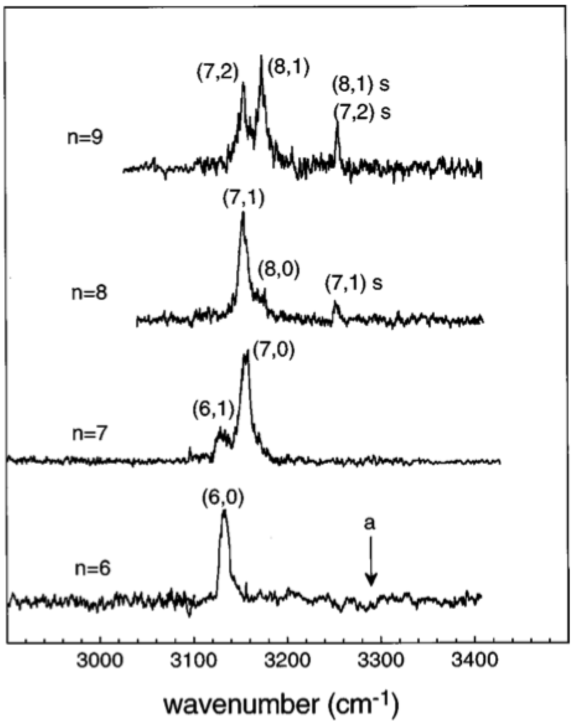

Figure 4. IR spectra of $Cl^{-}\cdots(HCCH)_n$ from n=6-9[12]

As the seventh ligand was added there was a change in the spectra. The major peak split into two and an additional minor peak was seen shifted less from the free acetylene than the major peak (Figure 4). This indicated the presence of two isomers in the mixture.

The first split of the major peak positioned one peak in the same range as the n=6 peak. The addition of the minor peak in combination with this seemed to indicate that a second solvation shell had formed (the first six ligands still in the first solvation shell) with the seventh being further away and not bonding directly to the ion. It was thought that due to it being situated further away from the ion centre it was interacting less strongly. Therefore its binding energy was closer to that of a free acetylene than those in the first solvation shell. The proposed structures of the two isomers can be seen in Figure 5.

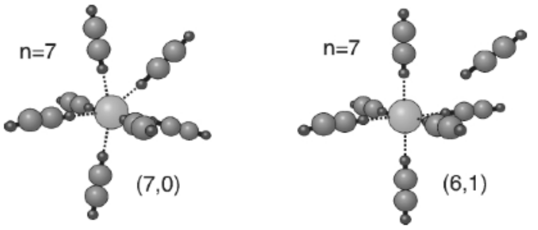

Figure 5. n=7 structures of $Cl^{-}\cdots(HCCH)_n$ *complex*[12]

The second split of the major peak was associated with the second isomer form. Its shift seemed to indicate that all seven of the ligands were inside the first solvation shell.

This trend of the second solvation shell and two isomers being detected continued with the addition of an eighth ligand: isomers of 8,0 and 7,1 formed. However, with the addition of a ninth ligand, the isomer with all ligands inside the first solvation shell disappeared due to steric crowding. Instead isomers of 7,2 and 8,1 were seen.

1.4.2 Bromide-acetylene anion clusters

Wild *et al.*[11] also studied the $Br^{-}\cdots(HCCH)_n$ complex using IR Spectroscopy. Similar to the studies of chloride-acetylene clusters, the step-wise addition of ligands in the $Br^{-}\cdots(HCCH)_n$ complex where n=1-8 has been explored. This complex also demonstrated the same solvation shell phenomenon. After six ligands a second solvation shell is seen and two isomeric forms of the complex are detected. This is seen by the same change in signal. A second, less-shifted minor peak forms, and the major peak splits into two. In addition, a similar even spacing of the ligands around the central ion as they are added to the cluster due to solvent-solvent interactions is observed in the structural determination.

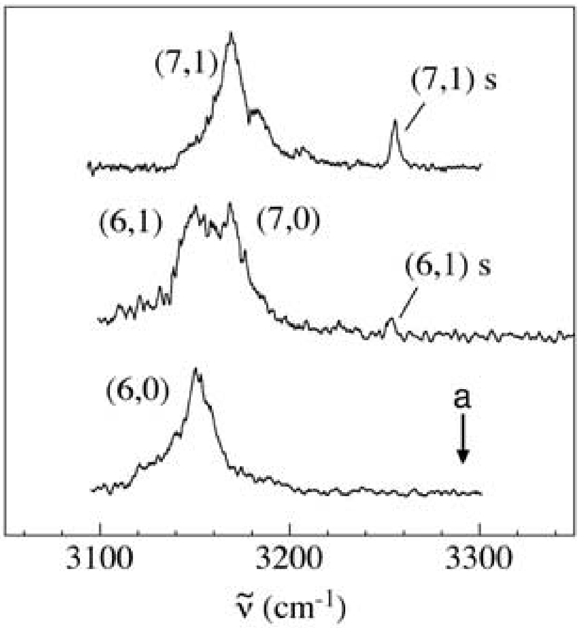

Figure 6. IR spectra of $Br^{-}\cdots(HCCH)_n$ *from n=6-8*[11]

In contrast to the chloride-acetylene complex, the bromide-acetylene complex's spectra suggest that the second solvation shell forms earlier than in the chloride-acetylene clusters, i.e. the first solvation shell of bromide is smaller. This is seen by the difference in the n=7 spectra between the two. In the chloride-acetylene n=7 spectrum, the 7,0 isomer peak is dominant but, in the bromide-acetylene n=7 spectrum, the 7,0 and 6,1 peaks are of equal size. This is further seen in the n=8 spectrum for bromide-acetylene where only one major peak is seen: the 7,1 isomer.

This observation is at odds with previous halide-ligand studies where usually the number of ligands in the first solvation shell increases as the halide ion size increases, and warrants further study.

1.4.3 *Ab initio* calculations

The *ab initio* calculations of halide-acetylene complexes have largely been performed by Botschwina *et al*.[13,14,15] In their work they performed extensive geometry optimisation of the complexes and predicted the ground state rotational constant, the dissociation energy, the band origin and equilibrium bond lengths. The optimised equilibrium bond lengths calculated by Botschwina for chloride-acetylene can be seen in Table 1.

Table 1. Optimised bond lengths for $Cl^{-}\cdots(HCCH)$ complex by Botschwina *et al* at multiple levels of theory[13,15]

	MP2/val aug-cc-pVQZ	**CCSD/val aug-cc-pVQZ**	**CCSD(T)/val aug-cc-pVQZ**	**CCSD(T) aug-cc-pV5Z**
$r(Cl...H_1)$/Å	2.2286	2.2886	2.2520	2.2521
$r(H_1\text{-}C_1)$/Å	1.0919	1.0875	1.0922	1.0919
$r(C_1\text{-}C_2)$/Å	1.2154	1.2056	1.2127	1.2118
$r(C_2\text{-}H_2)$/Å	1.0604	1.0607	1.0627	1.0623

Using large-scale CCSD(T) calculations, Botschwina predicted the equilibrium structures of the anion-complexes to be linear with a substantial energy barrier separating the two minima of the potential energy surface. The geometry also shows a strong distortion of the symmetry of the acetylene with a lengthening of the H_1-C_1 bond.

Further *ab initio* calculations have been performed on the neutral and anion fluoride-acetylene complex with one acetylene ligand by Quak[16]. This study explored the geometry optimisation of the complexes, as well as natural bond orbital (NBO) analysis and the prediction of potential energy surfaces of the two complexes. The geometry optimisation of the anion-cluster of fluoride-acetylene showed a linear structure with a distinct distortion in the bond lengths from the fluoride-hydrogen interaction. This interaction had caused the bond length of the hydrogen-carbon bond closest to the fluoride to lengthen (Figure 7). Through NBO analysis, hydrogen bonding between the fluoride and acetylene was indicated.

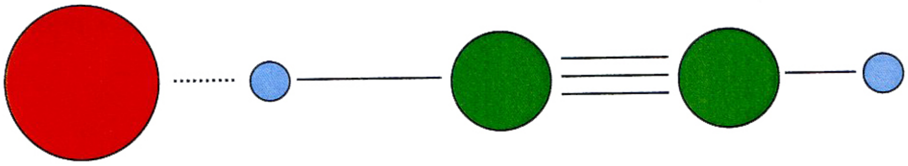

Figure 7. Schematic of the optimised geometry of $F^{-}\cdots(HCCH)$[16]

The geometry optimisation of the neutral complex showed two equilibrium geometries: a linear structure and a favoured T-shape structure. The linear structure had weaker interactions between the fluorine and the acetylene, with little distortion of the acetylene bond lengths and the species further apart compared to the anion linear geometry.

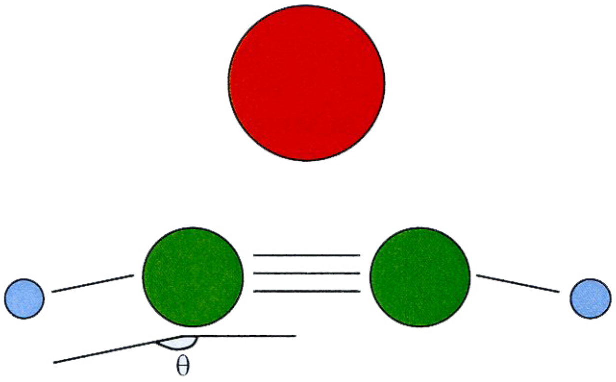

Figure 8. Schematic of the optimised geometry of T-shape $F\cdots(HCCH)$[16]

In the T-shape geometry, the fluorine atom is positioned near the triple bond of the acetylene which maximises the dispersion interaction between the fluorine and the acetylene. The linear structure of the acetylene ligand is also changed as the hydrogen-carbon bonds are pushed away from the fluorine atom (Figure 8).

Further work by Wild *et al.*[17] was performed on the fluoride-acetylene complexes. In this work, structure for the $F^{-}\cdots(HCCH)_n$ complex where n=1-6 was predicted using *ab initio* calculations. These calculations predicted the formation of a solvation shell around the fluoride with hydrogen bonds, as seen in previous halide-acetylene work, as well as a distorted acetylene ligand (Figure 9).

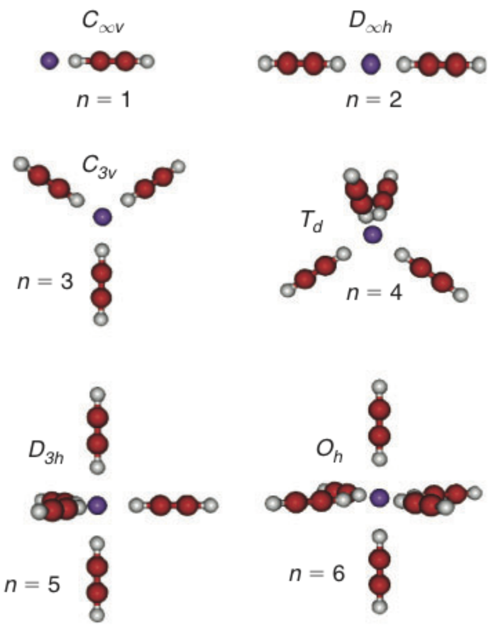

Figure 9. Predicted structures for the $F^{-}\cdots(HCCH)_n$ *clusters*[17]

A similar distortion of the acetylene has been seen in *ab initio* calculations by Wild *et al*[18] on the bromide-acetylene complex. In the minimum energy geometry calculated, a lengthening of the carbon-hydrogen bond closest to the bromide was observed.

2 Methods

2.1 Time of flight anion photoelectron spectroscopy

The apparatus used in the Wild lab (Figure 10) is a Time of Flight Mass Spectrometer (TOF-MS) coupled to a Time of Flight Photoelectron Spectrometer (TOF-PES), which allows easy mass separation of ionic clusters prior to photodetachment of the cluster. Currently it is set for anion photoelectron spectroscopy. The apparatus is based on the TOF-MS by Wiley and McLaren.[19]

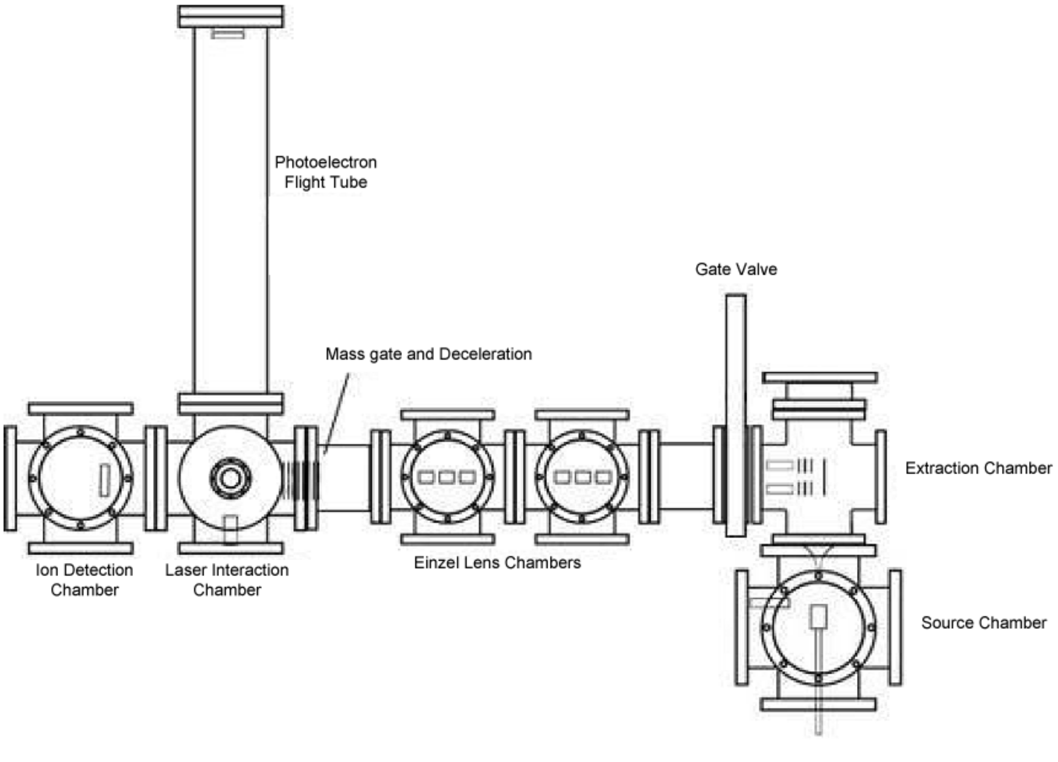

Figure 10. Schematic of the TOF-PES in the Wild lab[20]

2.1.1 Anion cluster selection

The first step of the procedure is creating the gas mixture. The source of the halide ions comes from CCl_4, Br_2CH_2, or CH_3I depending on which halide is being used to make the clusters. This is mixed with the acetylene gas and argon gas. The argon gas is used as a backing gas as well as a cooling gas: it causes collisions with the clusters to reduce the effects of hot bands (where the populations are spread into vibrational states other than the ground state). This provides vibrational cooling and results in spectra of a higher resolution.[21] This gas mixture is then pulsed into the source chamber.

The gas pulse then interacts with a pulsed electron beam to form the charged clusters and is then skimmed by a conical skimmer to form an ion beam that enters the extraction chamber is a mixture of anion, neutral and cation clusters. For anion-cluster selection, the clusters are exposed to a series of negatively-charged plates which cause the anions to be deflected down the time of flight tube. The cations are deflected away from the time of flight tube by the electric field and the neutral clusters are unaffected; continuing straight (Figure 11).

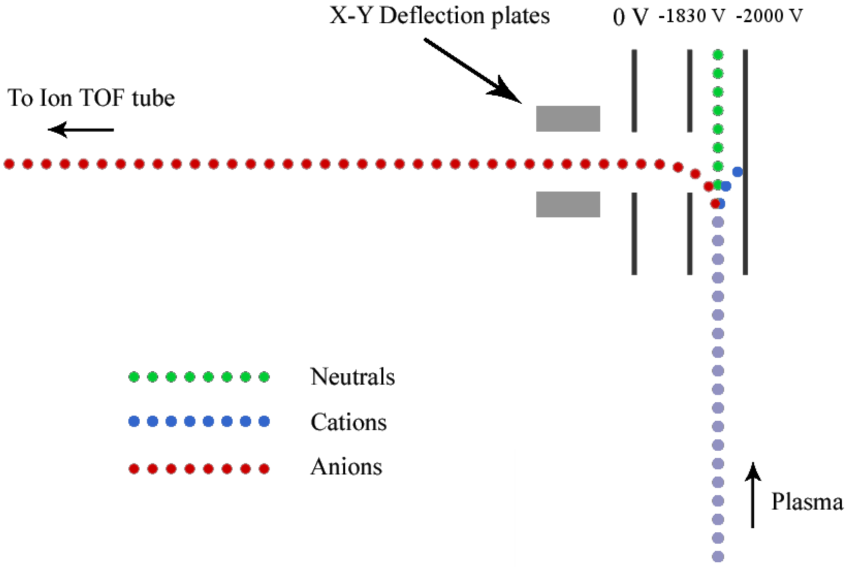

Figure 11. Diagram showing the anion selection in the extraction chamber of the TOF-PES[6]

2.1.2 Time of flight and mass selection

By deflecting the anion clusters with an electric field, it ensures all the anion clusters have the same kinetic energy when they are deflected down the time of flight tube. This can be understood by equation 3:

$$KE = qU \qquad \textbf{(3)}$$

where *KE* is the resulting kinetic energy of the clusters; *q* is the charge of the particle and; *U* is the voltage of the electric field. The electric field is constant and the charge of the clusters is uniform, therefore, all the anion clusters exit the region with the same kinetic energy.

As the clusters travel down the time of flight tube they have different velocities due to having different masses but the same kinetic energy (equation 4). Their velocity determines the time *t* that it takes for the individual clusters to travel down the time-of-flight tube of set length *d* (equation 5).

$$KE=\frac{1}{2}m_e v^2 \qquad \textbf{(4)}$$

$$v=\frac{d}{t} \qquad \textbf{(5)}$$

$$t=\frac{d}{\sqrt{(\frac{2\mathrm{KE}}{m})}} \qquad \textbf{(6)}$$

Therefore, the clusters spread out by mass and arrive at different times at the detector (equation 6). This provides some advantages when paired with photoelectron spectroscopy. The most obvious is the easy mass selection of the clusters prior to photoelectron spectroscopy which can lead to easier identification of the clusters and allow the step by step addition of ligands around the central ion to be more easily followed.

Other components in the TOF-MS interact with the ion beam to increase either the ion abundance or resolution of the spectra. The first are the X-Y deflection plates shown in Figure 11 and positioned in the extraction chamber in Figure 10. Using two sets of parallel charged plates and producing electric fields perpendicular to the ion beam path, the beam can be steered in either direction for optimal signal.[22]

After the X-Y deflection plates two sets of Einzel lenses are placed that focus the ion beam by use of a high negative potential. This is to ensure a more focused beam reaching the detector and to increase peak intensity and resolution.[22]

2.1.3 Photoelectron spectroscopy

The laser is a Nd:YAG laser with fundamental wavelength of 1064 nm. The fourth harmonic at 266 nm is utilised and is created by two beta barium borate (BBO) crystals in series. The first crystal produces 532 nm, while the second produces 266 nm. This laser interacts with the selected cluster, causing an electron to be ejected. The photoelectron is then deflected by a magnetic field down the photoelectron time-of-flight tube with a known kinetic energy.

The kinetic energy of the photoelectrons relates to the binding energy that is characteristic of particular energy levels and orbitals. In this manner, information about the photoelectron can be used to infer the structure changes as the cluster size increases, the different solvation shells and aid in structure determination of the clusters.

By using anion photoelectron spectroscopy, it is also possible to gain insight into the neutral potential energy surface by the anion to neutral transition.[9] This can provide further advantages to the study of complexes in comparison to looking at the same neutral potential energy surfaces by using traditional spectroscopy on neutral complexes. One very prominent advantage is the ability to look at neutral clusters that would otherwise be unavailable to other spectroscopic techniques due to a short lifespan because of their instability or high reactivity.[8]

2.1.4 Operating conditions

The mass spectra of X...$(HCCH)_n$ (X = Cl, Br, I) were taken over consecutive days with the new gas mixtures made in the afternoon and left to sit overnight to diffuse. Each was made with approximately 5% acetylene. Because of the similarities between the gas mixtures and the residues of previous gas mixtures remaining, the machine settings for optimal peak intensities were similar across all three gas mixtures. Table 2 shows basic settings for the TOF-PES for these experiments. For each gas mixture small changes were made to the settings to completely optimise for the desired clusters.

Table 2 – Typical TOF-MS experimental conditions

X1|X2	070 V, 059 V		
Y1|Y2	-056 V, -059 V	AIG1	2 x 10^{-5} Torr
Einzel	-57 V, -95 V	AIG2	2 x 10^{-6} Torr
Gas	216 V	AIG3	7 x 10^{-8} Torr
e^-	4.16 A, -456 eV, -180 V		
TOF	704 μs	Beam energy	2000 V

X1|X2 and Y1|Y2 are the voltages across the parallel sets of X-Y deflection plates and the Einzel setting is the potential applied to the two Einzel lenses in the time-of-flight tube. The gas setting is the voltage applied to the nozzle and by changing the voltage the amounts of certain clusters formed can be changed. The setting above of 216 V favours the smaller clusters and could be adjusted to increase the larger clusters when spectra are taken. The e^- setting shows the electron filament current, the electron energy and the electron Einzel lens voltage. The TOF value is the timing of the pulse sent to the extractor and repeller with respect to pulsing the nozzle. Beam energy is the voltage on the plates in the extraction chamber (Figure 11) that deflects the anions down the time of flight tube. Finally AIGX (X=1, 2, 3) is the working pressure at the time. Fluctuations or too high readings can indicate a leakage or instability in the nozzle.

2.2 Modifications to the TOF-PES

To further improve the resolution of the TOF-PES spectra, a new magnet was designed. At present the TOF-PES uses a pulsed solenoid magnet to deflect the detached photoelectrons down the time-of-flight tube. A number of disk shaped permanent magnets with strengths of around 5000 Gauss were attached to the end of individual poles and a device made to allow the poles to be positioned in the machine. The strength of 5000 G was determined by a similar magnet set up by Cheshnovsky *et al.*[23] Figure 12 shows the planned set up of the new magnet. The design and the magnet on the end of a longer pole allows the magnets to be interchanged easily during experiments without having to open the rest of the machine up to atmosphere.

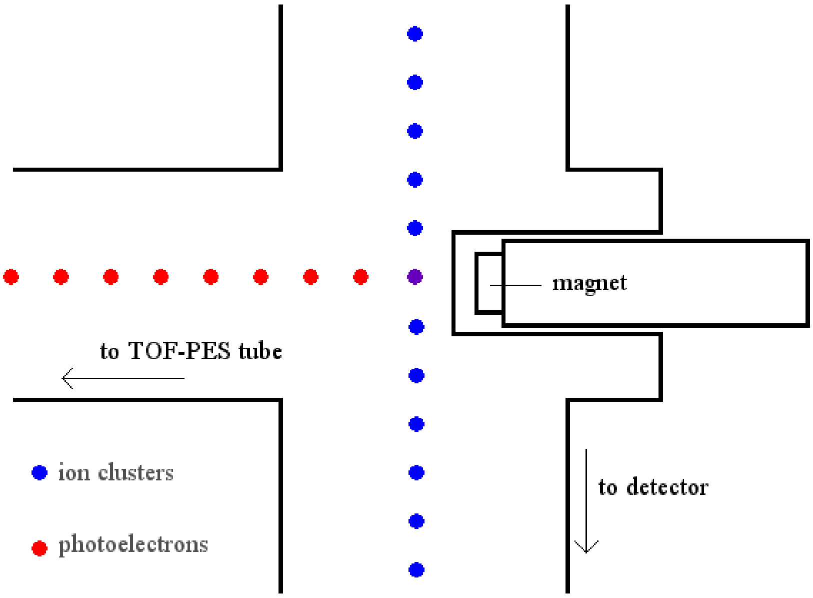

Figure 12. Diagram showing the deflection of the photoelectrons by the magnet

Initial tests of the magnet showed no photoelectrons being detected. It is hypothesised that the magnets were too strong and thus the coupling between the weaker magnetic field along the photoelectron flight tube and the strongly divergent magnetic field of the permanent magnet was not able to occur and form the required bottleneck (Figure 13).

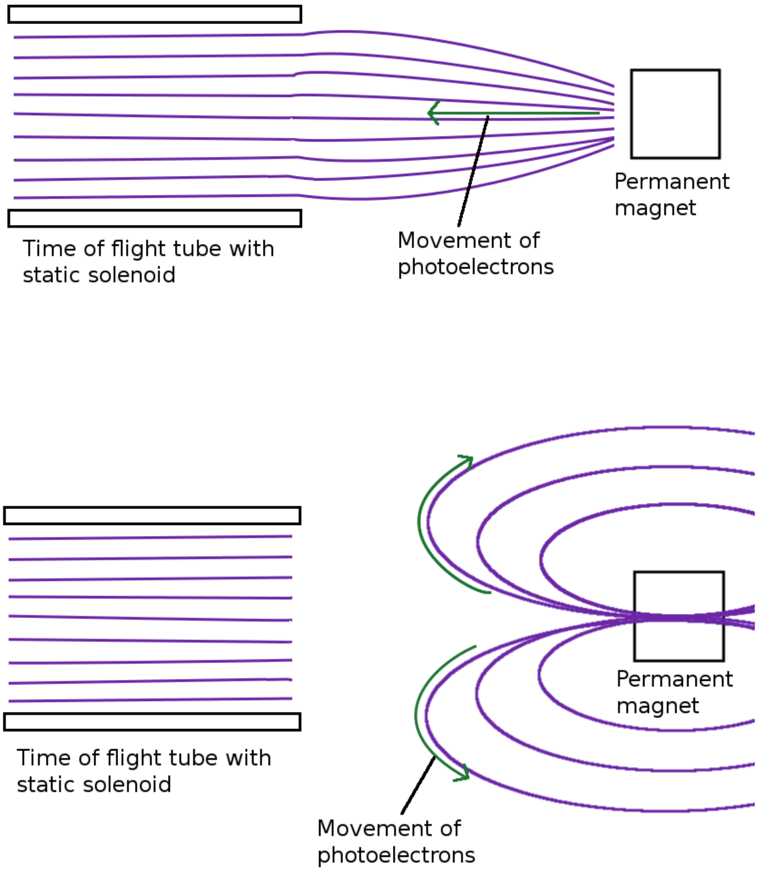

Figure 13. Diagram showing the desired bottle neck magnetic field coupling (top) and the strong divergent magnetic field of the 4000 Gauss magnets (bottom).

In order to combat this, lower strength magnets were ordered and fitted to poles for use with the machine. In the interim the magnet was replaced with the previous solenoid magnet. However due to issues later discussed with the ion beam and resulting photoelectron spectra, the new permanent magnets were not able to be tested.

2.3 *Ab initio* calculations

The *ab initio* calculations have been performed using the programs ORCA[24] and Gaussian 09.[25] The clusters are optimised using Møller Plesset 2nd order perturbation theory (MP2)[26] and Coupled-cluster single double (triple) (CCSD(T))[27] both with Dunning's augmented correlation consistent polarised valence double and triple zeta basis sets (aug-cc-pVXZ, where X = D, T).[28, 29, 30, 31]

The anion species of chloride-, bromide- and iodide-acetylene have previously been studied by Botschwina *et al.*[13,14] using CCSD(T) up to aug-cc-pV5Z. This project's set of *ab initio* calculations builds on the previous work to also look at the neutral species for all three halogen-acetylene clusters. Therefore for consistency in results the anion calculations were repeated to the same level of theory as the neutral species using ORCA. Bromide-acetylene calculations were performed to CCSD(T)/aug-cc-pVTZ without Effective Core Potential (ECP) approximations and with ECP approximations to MP2/aug-cc-pVTZ PP to compare the effects of ECP approximations on the geometry optimisation of bromide-acetylene.

Iodide-acetylene was only optimised to MP2/aug-cc-pVXZ (X= D, T) due to lack of time and problems with ORCA and Gaussian 09. These calculations were done with ECP approximation due to the size of the iodide ion and requirements of the basis sets used.

Following the geometry optimisations, the harmonic vibration frequency modes of the species were analysed to ensure there were no imaginary frequencies which would indicate a transition state and not a minimum. This was performed at all levels of theory as the geometry optimisations.

One-dimensional scans have been performed using Gaussian 09, on two of the vibrational modes found in the previous calculation: the rX-HCCH stretch and the θX-HCCH bend. The geometry of the cluster was allowed to optimise at each step of the 1D scan.

For these scans, the distance rX-HCCH has been measured from the halide and the centre of the acetylene molecule, using dummy atoms at the centre point as a reference. The angle scan is also with reference to a central dummy atom where the halide swings around the acetylene molecule (Figure 14). Using this method, a linear geometry would be observed at 90°. However, in the angle scan results these angles have been changed to reflect a linear geometry at 0° and 180°.

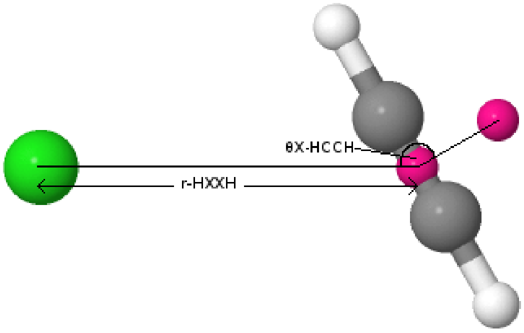

Figure 14. The halide swinging around the centre of the acetylene with reference to dummy atoms during the angle scan

Natural Bond Orbital analyses were also performed using Gaussian 09 to determine the nature of the bond between the acetylene and the halide atom by identifying the electron transfers between the orbitals of the two units.[32] This was compared to the NBO analysis of the bare acetylene molecule, and also with a negative point charge replacing the anion, to ensure the electron delocalisations were not solely due to polarisation.

3 Experimental results

3.1 Mass spectra

The mass spectra are presented in the order that the experiments were performed. Despite flushing the gas mixing chamber with argon between experiments, remnants of the gas mixtures appear in the consequent mass spectra. These other halide peaks are useful for calibration purposes of the mass spectra as known masses that can be usually easily found in the experimental spectra.

3.1.1 $Br^{-}\cdots(HCCH)_n$

Figure 15 shows the region of $Br^{-}\cdots(HCCH)_n$ clusters in a mixture of dibromomethane and acetylene. Figure 16 shows the larger $Br^{-}\cdots(HCCH)_n$ clusters as well as mixed species formed in the gas mixture. Beyond this point, a series of clusters of bromide with dibromomethane and acetylene is seen, covering any further larger clusters of $Br^{-}\cdots(HCCH)_n$.

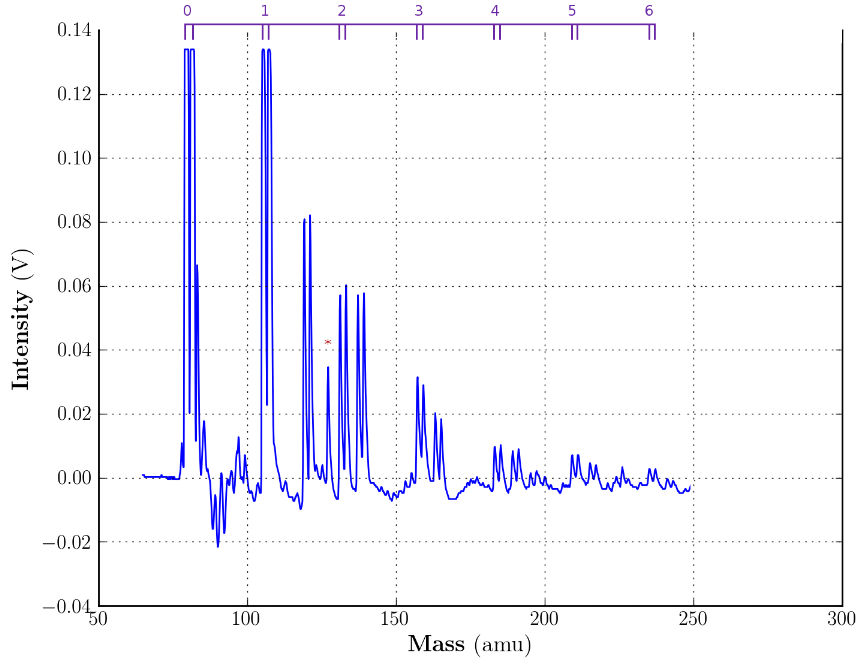

*Figure 15. Mass spectrum of bromide and its clusters with acetylene. The $Br^{-}\cdots(HCCH)_n$ series is marked purple. The I^{-} signal is marked with *. The Br^{-} and $Br^{-}\cdots(HCCH)$ peaks are cut off to show the smaller intensity peaks.*

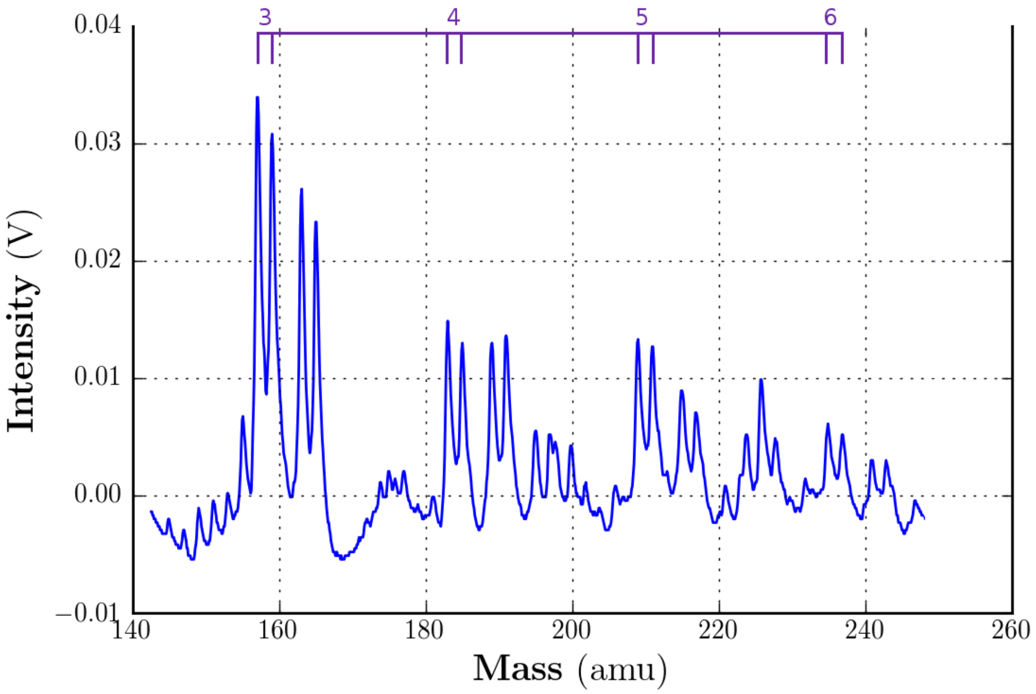

Figure 16. Larger clusters of $Br^{-}\cdots(HCCH)_n$ *(n=3-6). Larger clusters of* $Br^{-}\cdots((CH_3)_2CO)(HCCH)_n$ *and other clusters can also be seen.*

Due to the nature of the acetylene gas supply (acetylene dissolved in acetone) clusters with acetone and acetylene are also observed in the mass spectra: $Br^{-}\cdots((CH_3)_2CO)(HCCH)_n$ and $Br^{-}\cdots((CH_3)_2CO)_n$. $Br^{-}\cdots Ar$ is also seen due to using argon gas as the backing gas.

3.1.2 $I^{-}\cdots(HCCH)_n$

In Figure 17 the mass spectrum shows the region of $I^{-}\cdots(HCCH)_n$ clusters formed in a mixture of iodomethane and acetylene as well as remnants of the previously measured $Br^{-}\cdots(HCCH)_n$ clusters. Figure 18 shows the larger clusters of $I^{-}\cdots(HCCH)_n$. There are also peaks assigned to $I^{-}\cdots Ar$, $I^{-}\cdots((CH_3)_2CO)(HCCH)_n$ and $I^{-}\cdots((CH_3)_2CO)_n$. This is followed by a series of clusters of iodide with iodomethane and acetylene.

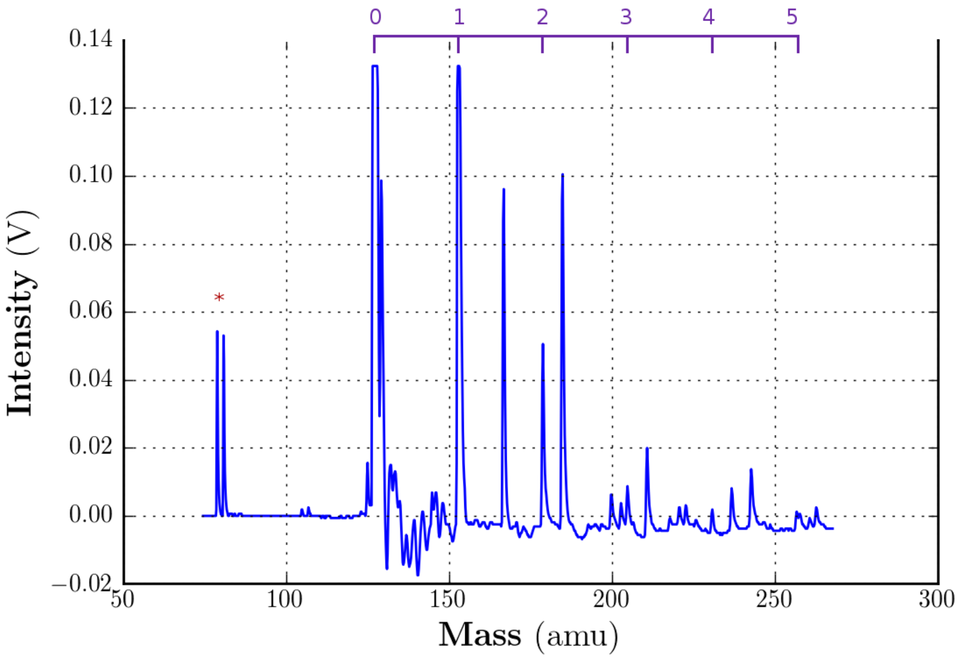

Figure 17. Mass spectrum of iodide and its clusters with acetylene. The $I^{-}\cdots(HCCH)_n$ *series is marked in purple. The* Br^{-} *signal is marked with *. The* I^{-} *and* $I^{-}\cdots HCCH$ *peaks are cut off to show the weaker species. Remnants of the previous* $Br^{-}\cdots(HCCH)_n$ *gas mixture can be seen at the left.*

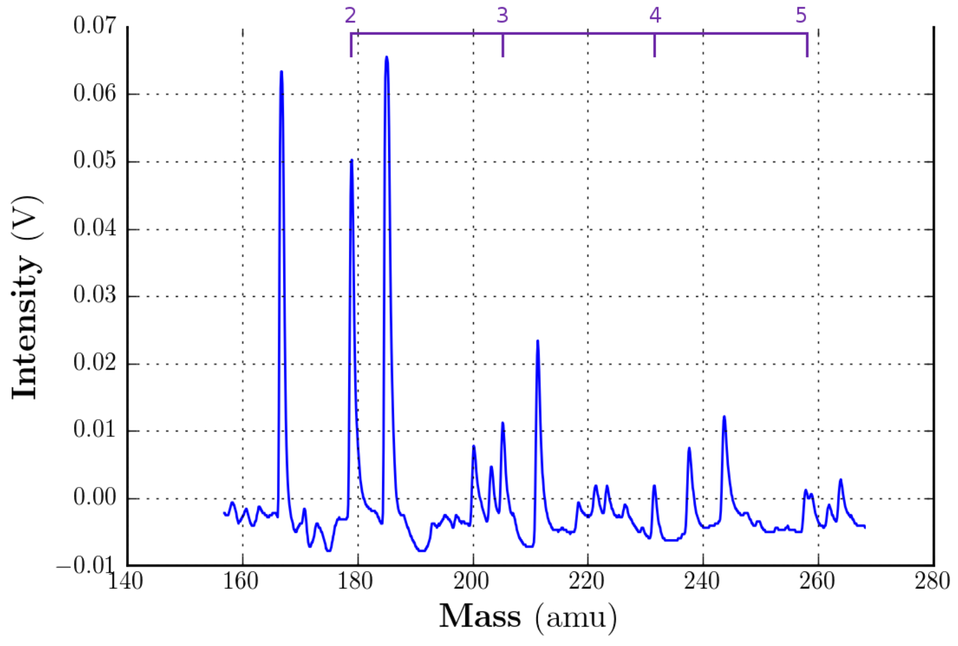

Figure 18. Larger clusters of $I^{-}\cdots(HCCH)_n$ *(n=2-5). Other clusters are also seen. The* $I^{-}\cdots(HCCH)_n$ *series is marked in purple.*

3.1.3 $Cl^{-}\cdots(HCCH)_n$

In Figure 19 the mass spectrum shows the region of $Cl^{-}\cdots(HCCH)_n$ clusters formed in a mixture of carbon tetrachloride and acetylene as well as remnants of the previously measured $Br^{-}\cdots(HCCH)_n$ and $I^{-}\cdots(HCCH)_n$ clusters. There are also peaks of $Cl^{-}\cdots Ar$, $Cl^{-}\cdots((CH_3)_2CO)(HCCH)_n$ and $Cl^{-}\cdots((CH_3)_2CO)_n$.

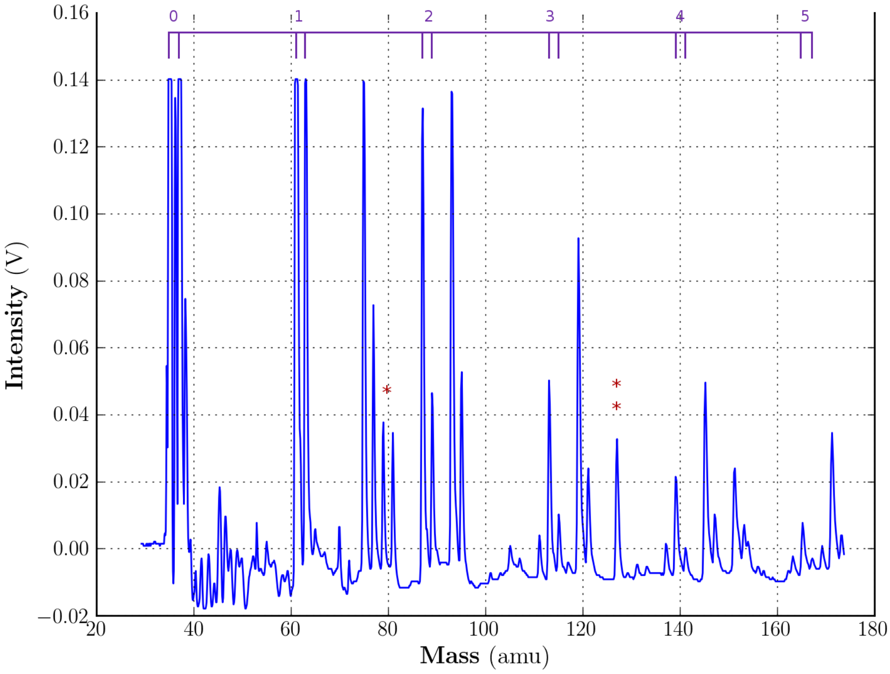

*Figure 19. Mass spectrum of chloride and its clusters with acetylene. The $Cl^{-}\cdots(HCCH)_n$ series is marked in purple. The Cl^{-} and $Cl^{-}\cdots HCCH$ peaks are cut off to show the weaker species. Remnants of the previous $Br^{-}\cdots(HCCH)_n$ and $I^{-}\cdots(HCCH)_n$ gas mixtures can be seen marked with * and ** respectively*

3.2 Photoelectron Spectra

Preliminary photoelectron spectra of the Br···(HCCH)$_n$ gas mixture were taken early in the year. Only the bare neutral atoms and 1:1 clusters with acetylene and argon were taken as larger clusters were not able to be found at the time. The photoelectron spectra of Br, Br···(HCCH) and Br···Ar are shown in Figures 20 to 22.

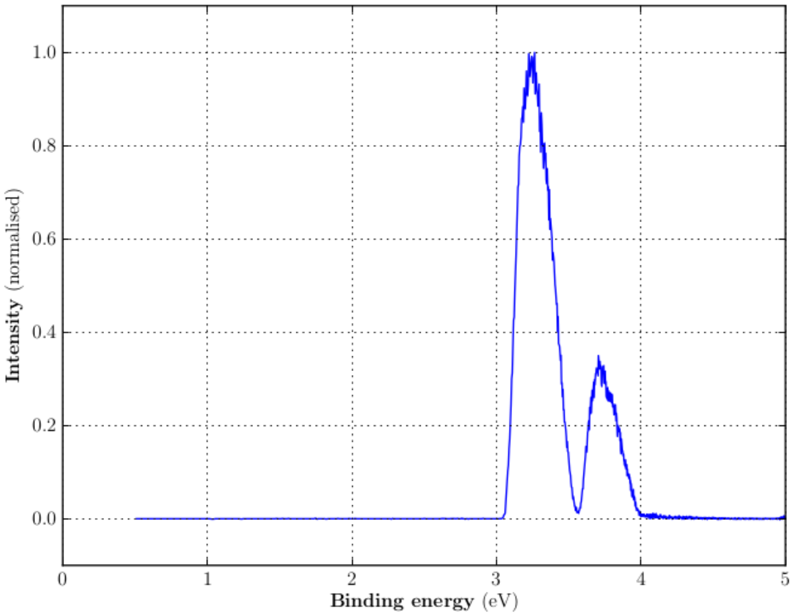

Figure 20. Photoelectron spectrum of Br

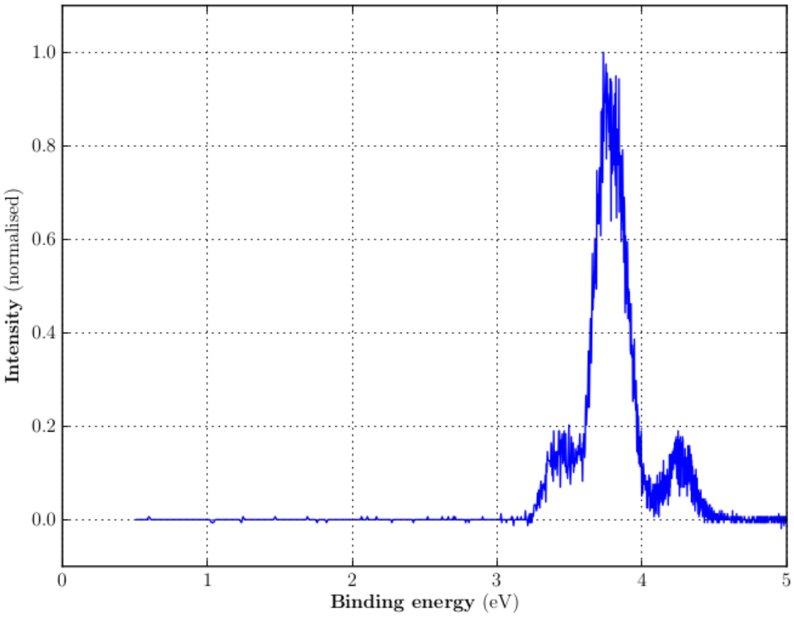

Figure 21. Photoelectron spectrum of Br···(HCCH)

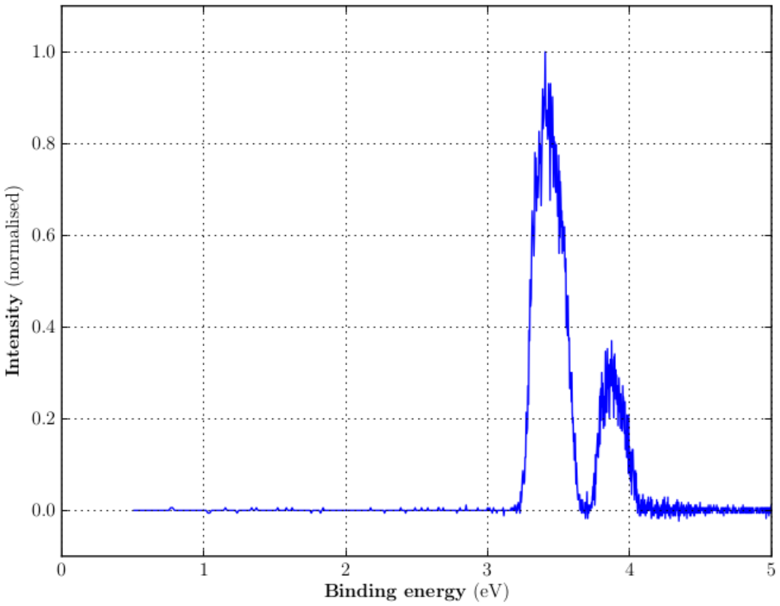

Figure 22. Photoelectron spectrum of Br$^-$···Ar

3.3 Experimental discussion

During preliminary experiments, ion clusters were not able to be seen in the mass spectra. By pumping out the gas mixing station and effectively removing the majority of the acetylene, X$^-$···Ar clusters were seen. This lead to the conclusion that the acetylene was somehow affecting the nozzle and not allowing clusters to be created.

The problem seemed to be due to the method of creating the gas mixture. First a small amount of the halide is let into the evacuated gas mixing chamber. This is followed by an amount of acetylene and then the remainder of the chamber is filled with argon. It was thought that due to this method, the acetylene and argon gas were forming a stratified gas mixture rather than diffusing to form a uniform mixture. Therefore only the acetylene was being pulsed through the gas nozzle. It has been observed previously that if the gas mixture is left overnight, the ion peaks seen in the mass spectra increase or 'grow in' over time. This observation enforces the hypothesis of gas mixture stratification and the layers diffusing over time to create more clusters.

By repeated tests it was found that a usable acetylene gas mixture was made by adding approximately 5% acetylene and letting it diffuse overnight. It was also important for the gas mixture to not be let up into the nozzle until the next day to ensure as much diffusion of the gas mixture as possible and to avoid any blockage by acetylene.

3.3.1 Mass spectra

In all of the mass spectra taken, there is a change in the base line with a significant amount of noise after all of the largest peaks. This is thought to be due to the large amount of ions hitting and saturating the detector causing a reduction in response. This effect is increased in the optimisations done for the mass spectra – particularly increasing the beam energy and raising the detector so a maximum peak intensity was found.

There is a change in the peak shape for each different halide cluster used across the mass spectra taken. This is due to differences in the natural abundance of isotopes that is reflected in the shape and ratio of the peaks of each halide. Bromide is seen to have a 1:1 ratio of isotopes with the two peaks in the doublet being the same height; chloride has a 1:3 ratio and iodide as a mono-isotopic element has a single peak for each of its observed clusters.

Also seen in all of the mass spectra was a series of clusters $XY_m\cdots(HCCH)_n$ (X = Cl, Br, I; Y = CCl_4, Br_2CH_2, CH_3I). In the spectra shown, only the first series of $X(HCCH)_n$ clusters are shown with the second series of $XY\cdots(HCCH)_n$ clusters directly following. The presence and intensity of the $XY_m\cdots(HCCH)_n$ clusters (Figure 16) seems to be due to the amount of starting halide material that is in the gas mixture despite using about 0.2% in the mixture. The second series of $XY\cdots(HCCH)_n$ clusters covers further clusters of the first series, limiting the amount of larger clusters that are detectable by mass spectra. This inhibits the ability to further explore the solvation phenomenon as only clusters up to $X^{-}\cdots(HCCH)_6$ are seen when previous research indicates that upwards of 7 acetylene ligands are needed to form a second solvation shell.[11,12]

3.3.2 Photoelectron spectra

On comparison of the photoelectron spectra (Figures 20 to 22) the expected shift in binding energy from the bare bromide can be seen upon addition of ligands. The acetylene shift is greater than the argon, due to the difference in the strength of the solvent-solute interaction: bromide forms a stronger bond with acetylene.

Prior to the first expected peak in the $Br\cdots(HCCH)$ spectra is an extra peak that is thought be a hot band resolving in the spectrum. This additional peak appears in all other $Br\cdots(HCCH)$ photoelectron spectra taken in this period but unfortunately it was not able to be further explored during later periods of experiments due to issues with the TOF-PES.

Attempts were made at taking spectra of $Br\cdots(HCCH)_2$ were unsuccessful due to low intensity of the ion clusters and hence low amounts of photoelectrons being produced. Larger clusters resulted in the same problem. However, mass spectra taken with later gas mixtures (Figures 15 to 19) showed much greater intensities and would have allowed for larger clusters to be found using photoelectron spectroscopy.

3.3.3 Nozzle instability

During the experimental period, there were many problems with the TOF-PES. At the beginning of the experimental period, there was a noticeable instability of the gas nozzle, which was observed by the peak intensity in the mass spectra fluctuating and disappearing after a period of constant pulsing of the gas mixture. This was remedied by thorough cleaning of the nozzle via sonication and soaking parts of the nozzle in acetone before reassembling it. While the resulting stability was not ideal, it was noticeably better than before. Possible reasons behind the instability could be the material of the sealing poppet inside the nozzle; previously it has been made of a softer material and has since been replaced with a harder poppet. Combined with the acetylene it is possible that the nozzle is not pulsing properly. It is also possible that the nozzle needs a full replacement. There are plans to eventually replace the current nozzle with a new piezo nozzle that should provide better gas density and better reproducibility between pulses as seen by Proch and Trickl*.

3.3.4 Ion beam deflection

Following the remedying of the nozzle instability, there was an incident with the pressurised air in the Bayliss Building which resulted in the valves shutting down and the TOF-PES turning off. Resulting from this incident, it was observed that the ion beam now deflected upwards. This was seen in the mass spectra by a dramatic decrease in the ion intensity that was remedied by raising the detector up to be in the path of the deflected ions (Figure 23).

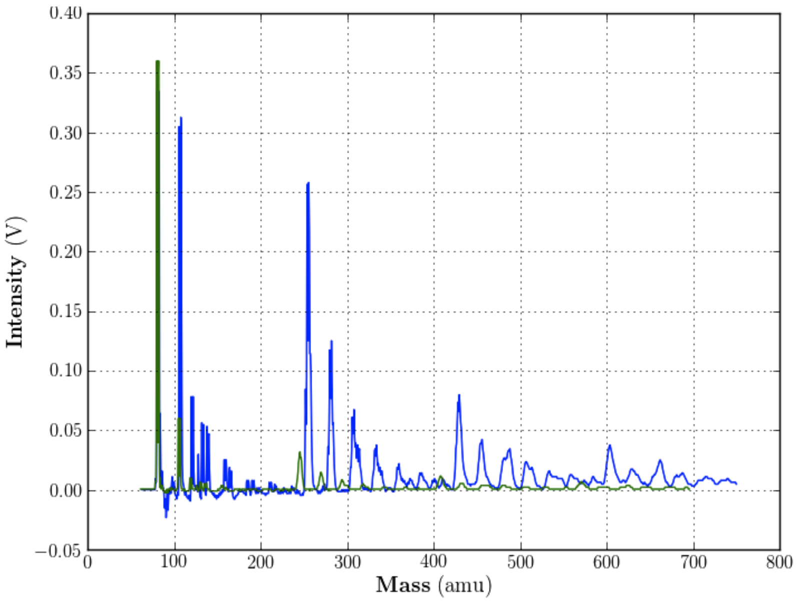

Figure 23. A full mass spectrum of $Br^-\cdots HCCH$ showing the change in peak intensity and ion detection at different detector positions (blue = 30mm, green = 44mm/central)

In previous experiments using the TOF-PES, the beam energy was sufficient for experiments set at 1000 V. It was discovered that by raising the beam energy to 2000 V the deflection of the ion beam decreased: the position of the detector for maximum peak intensity changed from 12 mm to 30 mm. The increase in the beam energy also superficially increased the overall intensity of the peaks; by increasing the beam energy, it increases the speed that the ion clusters hit the detector which increases the response.

While adjustment of the Einzel lenses and X/Y deflection plate settings were able to somewhat offset the effects of the ion beam deflection – when the Einzel lenses were turned off the beam deflected up more – the ion beam was not able to be corrected enough for photoelectron spectroscopy of the weaker clusters.

By changing the settings of the ion detector to instead detect neutral species, it was determined that photoelectrons were being detached from the clusters and neutral species were being created. However due to the deflection of the ion beam, not enough photoelectrons were being deflected down the photoelectron time-of-flight tube to be detected by photoelectron spectroscopy (Figure 24). To collect the photoelectrons, they need to be detached in the centre of the strong magnetic field, not near its periphery.

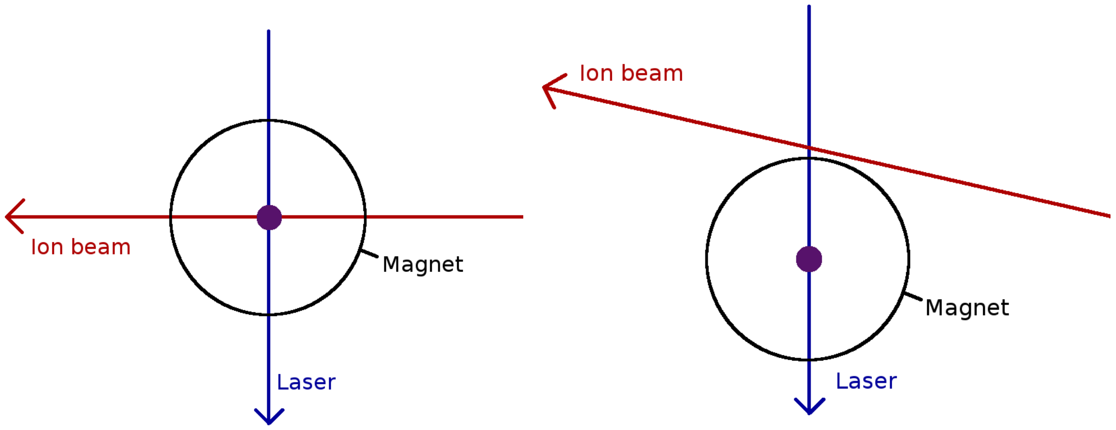

Figure 24. Diagrams showing the desired ion beam path (left) and the suspected beam deflection (right). Both intersect with the laser however the deflected beam passes above the magnet and therefore is not deflected down the time of flight tube.

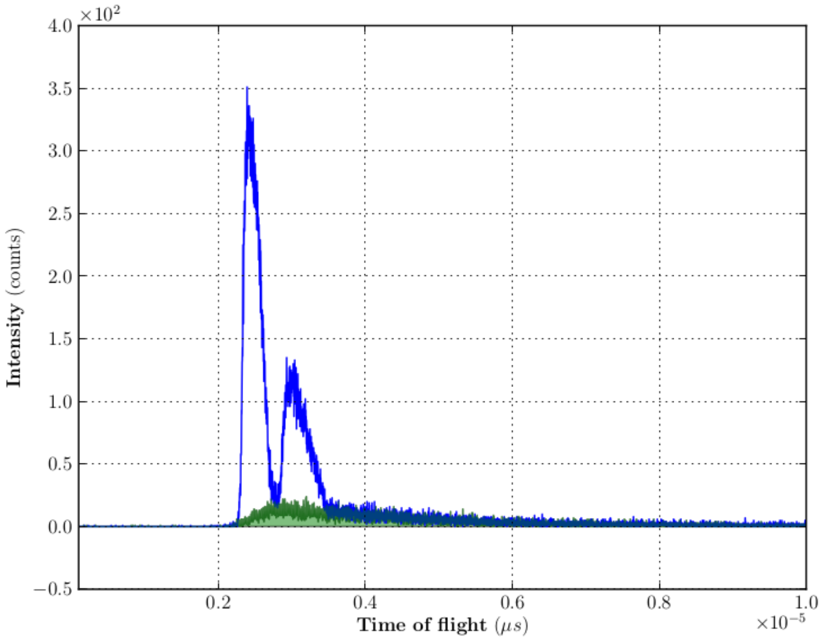

Figure 25. Photoelectron spectrum of Br⁻ (blue) and background (green)

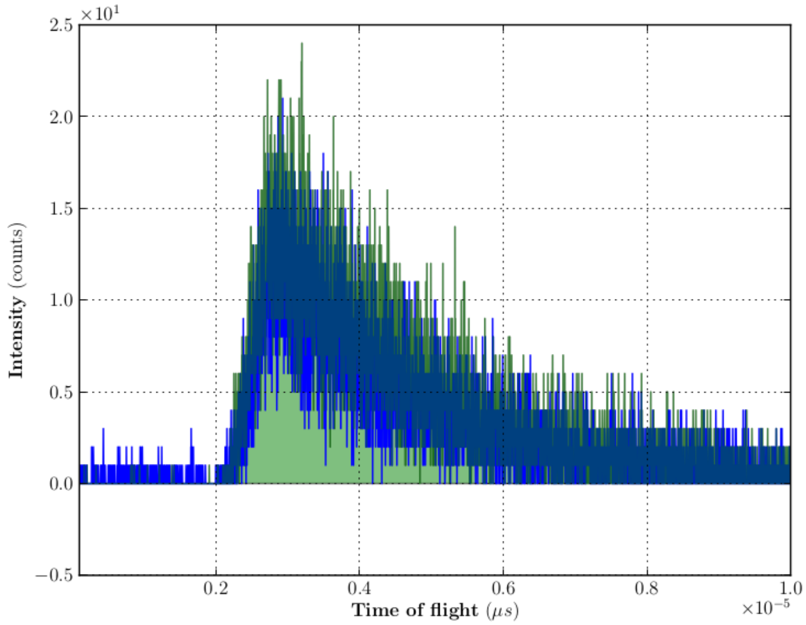

Figure 26. Photoelectron spectrum of Br⁻···HCCH (blue) and background (green)

Figure 25 shows the photoelectron spectrum of Br$^-$ with the measured background shown in green. This was measured with the detector at 44 mm and the beam energy at 1000 V. On the oscilloscope screen it was difficult to observe the photoelectrons from the Br^- anion and it was found using previously gathered laser timing data. It was thought that there was such a large amount of Br^- in the gas mixture that the amount of stray ions not deflected as much was sufficient for photoelectron spectroscopy.

This is in comparison to the $Br^-\cdots HCCH$ spectrum shown in Figure 26. The decrease in the amount of ions meant that there was not a sufficient amount intersected with the laser in the middle of the magnetic field.

The timing of the laser for $Br^-\cdots HCCH$ was known from previous experiments and attempts were made to find I^- with the same result. In both cases, no photoelectrons were able to be seen on the oscilloscope above the background. Even if peaks were able to be seen above the background in the photoelectron spectra, being unable to see the photoelectrons on the oscilloscope would have made it impossible to find later clusters whose timings were unknown, short of testing every 100 ns.

Previous experiments with the TOF-PES have required at least 10 mV of signal of ions in the mass spectrum to find the photoelectron spectra. If this held true for this series of experiments, we optimistically would have been able to find up to $X^-\cdots(HCCH)_4$ or even $X^-\cdots(HCCH)_5$ if the photoelectron spectrometer had been working at previous capacity.

4 *Ab initio* calculations

4.1 Optimised geometries

In addition to optimising the three halide-acetylene complexes, calculations were also performed on the bare acetylene molecule (Table 3). The data are used in comparison to the halide-acetylene complexes' data to show the change in properties of the acetylene by the presence and interactions with the halide.

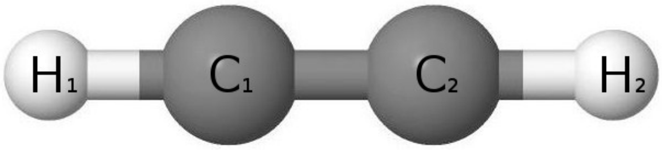

Figure 27. Schematic of the optimised geometry of HCCH

Table 3. Calculated data of bare HCCH. Values shown are the optimised geometry, vibration frequency wavenumbers with IR intensities in brackets (km mol^{-1}), zero point energies and final single point energies.

		MP2	
		pVDZ	**pVTZ**
r(H_1-C_1)/Å		1.081	1.066
r(C_1-C_2)/Å		1.231	1.212
r(C_2-H_2)/Å		1.081	1.066
ω_1/cm^{-1}	**σ**	3475 (<1)	3361 (<1)
ω_2/cm^{-1}		3379 (112)	3274 (115)
ω_3/cm^{-1}		1948 (<1)	1857 (<1)
ω_4/cm^{-1}	**π**	708 (118)	825 (118)
ω_5/cm^{-1}		512 (<1)	692 (<1)
zpe /kJ.mol^{-1}		16.1	16.5
E_e /hartree		-77.076004	-77.152132

4.1.1 Anion clusters

The anion complex $X^- \cdots HCCH$ is made up of a central anion with an acetylene molecule with an overall charge of -1 and a multiplicity of 1 (X = Cl, Br, I). The optimisations of the halide-acetylene complexes were done in order of increasing halide size, with the previously optimised geometry coordinates of F^-···HCCH being used as a starting point for the Cl^-···HCCH complex.[16] The Cl^-···HCCH coordinates were then subsequently used for the first Br^-···HCCH optimisation. For all anion complexes only one optimal geometry was found with no transition state geometries. The optimised geometry of the X^-···HCCH (X = Cl, Br, I) complexes are shown in Figures 28 to 30 with the accompanying physical data shown in Tables 4 to 6.

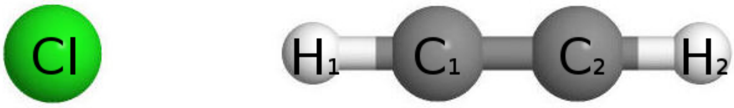

Figure 28. Schematic of the optimised geometry of Cl^-···HCCH complex

Table 4. Calculated data of Cl^-···HCCH complex at MP2/aug-cc-pVXZ and CCSD(T)/aug-cc-pVXZ (X = D, T).. Values shown are the optimised geometry, vibration frequency wavenumbers with IR intensities in brackets (km mol^{-1}), zero point energies and final single point energies.

	MP2		**CCSD(T)**	
	pVDZ	**pVTZ**	**pVDZ**	**pVTZ**
r(Cl...H_1)/Å	2.295	2.264	2.323	2.287
r(H_1-C_1)/Å	1.107	1.094	1.109	1.095
r(C_1-C_2)/Å	1.237	1.218	1.235	1.216
r(C_2-H_2)/Å	1.080	1.064	1.085	1.067
ω_1/cm^{-1} σ	3438 (7)	3475 (9)	3380 (5)	3434 (10)
ω_2/cm^{-1}	3062 (879)	3071 (866)	3048 (842)	3057 (820)
ω_3/cm^{-1}	1895 (159)	1912 (162)	1919 (155)	1934 (163)
ω_4/cm^{-1}	145 (34)	149 (33)	151 (32)	164 (62)
ω_5/cm^{-1} π	868 (61)	913 (51)	854 (62)	902 (51)
ω_6/cm^{-1}	532 (42)	618 (47)	514 (41)	609 (46)
ω_7/cm^{-1}	145 (<1)	145 (<1)	143 (<1)	143 (<1)
zpe /kcal.mol^{-1}	16.6	17.1	16.5	17.0
E_e /hartree	-536.815593	-536.951065	-536.858411	-537.003828
$E_{e/BSSE}$ /hartree	-536.799954	-536.934549	-536.843193	-536.987594
D_0 /cm^{-1}	6076	6118	6038	6311

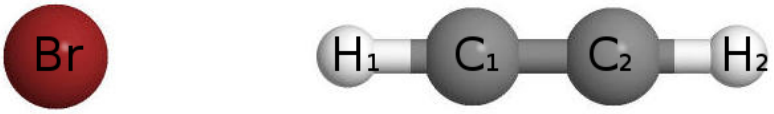

Figure 29. Schematic of the optimised geometry of Br$^-$···HCCH complex

Table 5. Calculated data of Br$^-$···HCCH complex at MP2/aug-cc-pVXZ and CCSD(T)/aug-cc-pVXZ (X = D, T). Values shown are the optimised geometry, vibration frequency wavenumbers with IR intensities in brackets (km mol^{-1}), zero point energies and final single point energies.

	MP2		**CCSD(T)**	
	pVDZ	**pVTZ**	**pVDZ**	**pVTZ**
r(Br...H_1)/Å	2.524	2.497	2.551	2.523
r(H_1-C_1)/Å	1.101	1.088	1.104	1.089
r(C_1-C_2)/Å	1.236	1.217	1.234	1.215
r(C_2-H_2)/Å	1.080	1.064	1.085	1.067
ω_1/cm^{-1} σ	3441 (6)	3477 (8)	3384 (3)	3427 (1)
ω_2/cm^{-1}	3140 (742)	3155 (721)	3117 (715)	3168 (704)
ω_3/cm^{-1}	1907 (118)	1923 (118)	1931 (116)	1962 (105)
ω_4/cm^{-1}	113 (11)	112 (11)	113 (10)	158 (10)
ω_5/cm^{-1} π	832 (61)	875 (51)	819 (62)	868 (52)
ω_6/cm^{-1}	531 (36)	619 (42)	514 (35)	611 (41)
ω_7/cm^{-1}	131 (<1)	133 (<1)	129 (<1)	128 (<1)
zpe /kcal.mol^{-1}	16.6	17.1	16.4	17.1
E_e /hartree	-2649.683486	-2649.875940	-2649.724857	-2649.926336
$E_{e/BSSE}$ /hartree	-2649.670429	-2649.862179	-2649.712224	-2649.912901
D_0 /cm^{-1}	6089	6095	6049	6321

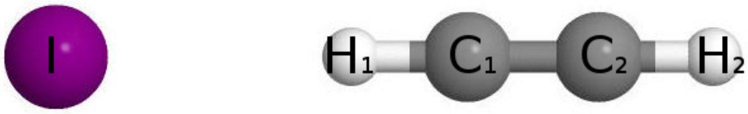

Figure 30. Schematic of the optimised geometry of I⁻···HCCH complex

Table 6. Calculated data of I⁻···HCCH complex at MP2/aug-cc-pVXZ (X = D, T). Values shown are the optimised geometry, vibration frequency wavenumbers with IR intensities in brackets (km mol^{-1}), zero point energies and final single point energies.

		MP2	
		pVDZ	**pVTZ**
r(I...H$_1$)/Å		2.785	2.671
r(H$_1$-C$_1$)/Å		1.097	1.084
r(C$_1$-C$_2$)/Å		1.235	1.217
r(C$_2$-H$_2$)/Å		1.079	1.064
ω_1/cm^{-1}	**σ**	3444 (4)	3481 (7)
ω_2/cm^{-1}		3199 (650)	3201 (684)
ω_3/cm^{-1}		1914 (93)	1930 (103)
ω_4/cm^{-1}		95 (5)	109 (5)
ω_5/cm^{-1}	**π**	806 (58)	891 (45)
ω_6/cm^{-1}		533 (32)	627 (40)
ω_7/cm^{-1}		127 (<1)	144 (1)
zpe /kcal.mol^{-1}		16.6	17.2
E$_e$ /hartree		-376.423967	-376.574531
E$_{e/BSSE}$ /hartree		-376.413669	-376.564617
D$_0$ /cm^{-1}		2533	1896

In all three halide-acetylene complexes there is a change in the geometry of the acetylene compared to the bare acetylene. The H$_1$-C$_1$ bond length increases, pulling the hydrogen closer to the halide. As the halide is changed from Cl to Br to I, the change in the H$_1$-C$_1$ bond length decreases and the distance between the acetylene and halide increases.

For each complex there are 10 vibrational frequencies: four individual σ vibrational frequencies (ω_1 to ω_4) and three pairs of degenerate π vibrational frequencies (ω_5 to ω_7).

These calculated values for all three complexes can be compared to previous calculations done by Botschwina *et al.*[13,14,15] Tables 7 to 9 compare the highest level of *ab initio* calculations performed in this series to the highest performed by Botschwina *et al.*

Table 7. Comparison of CCSD(T)/aug-cc-pVTZ (Table 4) with CCSD(T)/aug-cc-pV5Z calculations by Botschwina and Oswald[13] of $Cl^{-}\cdots HCCH$ complex

		CCSD(T)/aug-cc-pVTZ	CCSD(T)/aug-cc-pV5Z
r(Cl...H_1)/Å		2.287	2.252
r(H_1-C_1)/Å		1.095	1.092
r(C_1-C_2)/Å		1.216	1.212
r(C_2-H_2)/Å		1.067	1.062
ω_1/cm^{-1}	**σ**	3433	3459
ω_2/cm^{-1}		3056	3065
ω_3/cm^{-1}		1934	1949
ω_4/cm^{-1}		164	154
ω_5/cm^{-1}	**π**	902	917*
ω_6/cm^{-1}		609	599*
ω_7/cm^{-1}		143	146*
E_e /hartree		-537.003681	-537.055695*

*Data from a different set of calculations at CCSD(T)/aug-cc-pVQZ[15]

Table 8. Comparison of CCSD(T)/aug-cc-pVTZ (Table 5) with CCSD(T)/avqz calculations by Botschwina and Stoll[14] of $Br^{-}\cdots HCCH$ complex

	CCSD(T)/aug-cc-pVTZ	**CCSD(T)/avqz**
r(Br...H_1)/Å	2.523	2.480
r(H_1-C_1)/Å	1.089	0.086
r(C_1-C_2)/Å	1.215	1.212
r(C_2-H_2)/Å	1.067	1.063
ω_1/cm^{-1} σ	3427	3465
ω_2/cm^{-1}	3167	3147
ω_3/cm^{-1}	1962	1959
ω_4/cm^{-1}	158	117
ω_5/cm^{-1} π	867	880
ω_6/cm^{-1}	611	602
ω_7/cm^{-1}	128	132
E_e /hartree	-2649.926336	-2649.976748

Table 9. Comparison of MP2/aug-cc-pVTZ (Table 6) with CCSD(T)/PP calculations by Botschwina and Stoll[14] of $I^{-}\cdots HCCH$ complex

	MP2/aug-cc-pVTZ	**CCSD(T)/PP**
r(I...H_1)/Å	2.671	2.763
r(H_1-C_1)/Å	1.084	1.081
r(C_1-C_2)/Å	1.217	1.211
r(C_2-H_2)/Å	1.064	1.063
ω_1/cm^{-1} σ	3481	3468
ω_2/cm^{-1}	3201	3214
ω_3/cm^{-1}	1930	1970
ω_4/cm^{-1}	109	95
ω_5/cm^{-1} π	891	852
ω_6/cm^{-1}	627	606
ω_7/cm^{-1}	144	120
E_e /hartree	-376.574531	-88.815108

Most values agree with their results which extend to much higher level basis sets than performed here. There is a significant difference in the vibrational frequency wavenumber ω_4 of the Br^-···HCCH complex: 157 cm^{-1} at aug-cc-pVTZ and 117 cm^{-1} in the avqz calculations. In previous calculations (MP2/aug-cc-pVXZ (X=D, T) and CCSD(T)/aug-cc-pVDZ), the value for ω_4 is closer to the value given by Botschwina.

There is also a difference in the single point energy of the I^-···HCCH complex that occurs in both sets of calculations here: -376.574531 hartree and -88.815108 hartree. This is due to using ECP approximation in the calculations. This will be looked at more in a later section in reference to Br···HCCH data comparisons between MP2/aug-cc-pVXZPP and MP2/aug-cc-pVXZ (X=D, T)

4.1.2 Neutral clusters

The neutral complex geometry optimisation was done with reference to previous optimisations of F···HCCH which found two neutral optimised geometries[16]. These were used as starting points for the X···HCCH geometry optimisations and the same was found for all three clusters (X = Cl, Br, I).

The first neutral geometry is the "neutral linear" shown in Figures 31 to 33 with corresponding data in Tables 10 to 12.

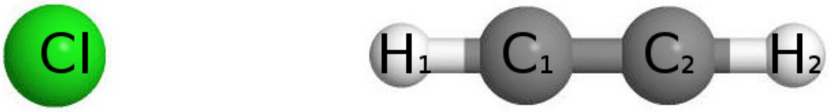

Figure 31. Schematic of the optimised geometry of Cl···HCCH neutral linear complex

Table 10. Calculated data of Cl···HCCH neutral linear complex at MP2/aug-cc-pVXZ and CCSD(T)/aug-cc-pVXZ (X = D, T). Values shown are the optimised geometry, vibration frequency wavenumbers with IR intensities in brackets (km mol^{-1}), zero point energies and final single point energies.

	MP2		**CCSD(T)**	
	pVDZ	**pVTZ**	**pVDZ**	**pVTZ**
r(Cl...H)/Å	2.899	2.927	2.919	2.952
r(H-C)/Å	1.081	1.066	1.086	1.069
r(C-C)/Å	1.232	1.213	1.230	1.211
r(C-H)/Å	1.081	1.066	1.085	1.068
ω_1/cm^{-1} σ	3470 (2)	3503 (1)	3419 (2)	3469 (2)
ω_2/cm^{-1}	3376 (170)	3413 (161)	3320 (166)	3373 (157)
ω_3/cm^{-1}	1946 (1)	1965 (1)	1969 (1)	1993 (1)
ω_4/cm^{-1}	58 (<1)	51 (<1)	**113 (<1)** [#]	**50 (<1)** [#]
ω_5/cm^{-1} π	719 (107)	762 (104)	713 (106)	756 (104)
ω_6/cm^{-1}	714 (106)	758 (104)	705 (106)	751 (104)
ω_7/cm^{-1}	524 (<1)	629 (1)	516 (2)	619 (1)
ω_8/cm^{-1}	521 (<1)	626 (1)	500 (<1)	618 (1)
ω_9/cm^{-1}	67 (<1)	57 (<1)	**-129** [*]	48 (<1)
ω_{10}/cm^{-1}	52 (<1)	40 (<1)	55 (<1)	45 (<1)
zpe /kcal.mol^{-1}	16.3	16.9	16.2	16.8
E_e /hartree	-536.669620	-536.801775	-536.717266	-536.859426
$E_{e/BSSE}$ /hartree	-536.668629	-536.800653	-536.716311	-536.859279
D_0 /cm^{-1}	5845	5968	5799	6374

[#] change in vibrational mode from MP2 vibrational frequencies explained in detail later.

[*] imaginary frequency

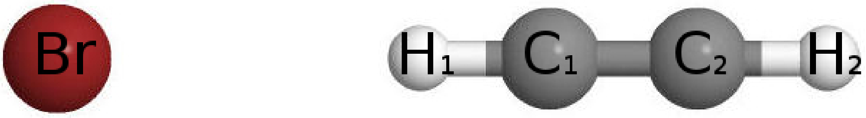

Figure 32. Schematic of the optimised geometry of Br···HCCH neutral linear complex

Table 11. Calculated data of Br···HCCH neutral linear complex at MP2/aug-cc-pVXZ and CCSD(T)/aug-cc-pVXZ (X = D, T). Values shown are the optimised geometry, vibration frequency wavenumbers with IR intensities in brackets (km mol^{-1}), zero point energies and final single point energies.

	MP2		**CCSD(T)**	
	pVDZ	**pVTZ**	**pVDZ**	**pVTZ**
r(Br...H)/Å	3.024	3.072	3.045	3.101
r(H-C)/Å	1.081	1.067	1.086	1.069
r(C-C)/Å	1.232	1.213	1.230	1.211
r(C-H)/Å	1.081	1.066	1.085	1.068
ω_1/cm^{-1} σ	3469 (2)	3501 (2)	3418 (3)	3467 (2)
ω_2/cm^{-1}	3375 (181)	3409 (169)	3319 (177)	3371 (165)
ω_3/cm^{-1}	1947 (2)	1965 (2)	1968 (2)	1992 (2)
ω_4/cm^{-1}	52 (<1)	45 (<1)	**41 (<1)** $^{\#}$	**42 (<1)** $^{\#}$
ω_5/cm^{-1} π	715 (103)	762 (101)	880 (86)	753 (102)
ω_6/cm^{-1}	712 (109)	759 (101)	654 (95)	752 (101)
ω_7/cm^{-1}	522 (1)	629 (1)	548 (18)	620 (1)
ω_8/cm^{-1}	520 (<1)	627 (1)	375 (5)	617 (1)
ω_9/cm^{-1}	57 (<1)	61 (<1)	**-381** *	61 (<1)
ω_{10}/cm^{-1}	43 (<1)	47 (<1)	135 (2)	36 (<1)
zpe /kcal.mol^{-1}	16.3	16.9	16.2	16.7
E_e /hartree	-2649.546630	-2649.736332	-2649.591036	-2649.789620
$E_{e/BSSE}$ /hartree	-2649.545547	-2649.735098	-2649.590008	-2649.788580
D_0 /cm^{-1}	5862	5976	5841	6192

$^{\#}$ change in vibrational mode from MP2 vibrational frequencies explained in detail later.

* imaginary frequency

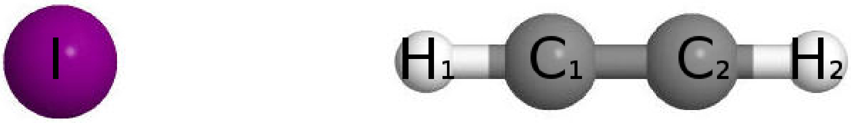

Figure 32. Schematic of the optimised geometry of I···HCCH neutral linear complex

Table 12. Calculated data of I···HCCH neutral linear complex at MP2/aug-cc-pVXZ (X = D, T). Values shown are the optimised geometry, vibration frequency wavenumbers with IR intensities in brackets (km mol^{-1}), zero point energies and final single point energies.

		MP2	
		pVDZ	**pVTZ**
r(I...H)/Å		3.175	3.128
r(H-C)/Å		1.081	1.066
r(C-C)/Å		1.230	1.213
r(C-H)/Å		1.081	1.066
ω_1/cm^{-1}	**σ**	3480 (3)	3502 (3)
ω_2/cm^{-1}		3375 (199)	3410 (198)
ω_3/cm^{-1}		2027 (3)	1967 (3)
ω_4/cm^{-1}		51 (<1)	55 (<1)
ω_5/cm^{-1}	**π**	722 (97)	771 (92)
ω_6/cm^{-1}		715 (105)	768 (99)
ω_7/cm^{-1}		533 (1)	634 (4)
ω_8/cm^{-1}		529 (<1)	633 (3)
ω_9/cm^{-1}		57 (<1)	77 (<1)
ω_{10}/cm^{-1}		40 (<1)	69 (<1)
zpe /kcal.mol^{-1}		16.5	17.0
E_e /hartree		-376.300802	-376.374035
$E_{e/BSSE}$ /hartree		-376.299670	-376.372932
D_0 /cm^{-1}		2531	1861

In all three neutral linear acetylene complexes, the halogen atom is further away from the acetylene molecule in comparison with the anion complexes. This is due to the difference in intermolecular forces between the anion-acetylene and neutral-acetylene. In the anion-acetylene complex there is the stronger ion-quadrupole and ion-induced dipole intermolecular forces. In comparison, because of the neutral central atom it is the weaker van der Waals interactions in the neutral-acetylene complexes. The increased distance and decreased interaction between the halogen and acetylene causes the linear distortion of the acetylene to be decreased: it is barely changed from the bare acetylene geometry. This is seen in the intensity of the intramolecular stretching mode ω_2 being greatly decreased and an overall shift in the C-H stretching modes ω_1 and ω_2.

It is also noticed that the degenerate vibrations of the neutral linear complexes (ω_5 to ω_{10}) are not degenerate in frequency as in the anion complexes. This results in some of the modes being reordered in the calculation results and the vibrational degeneracy not being as obvious, especially in the lower wavenumber vibrations. This may be due to a very shallow minimum of the linear-neutral complex which is seen later in the 1D potential energy scans.

In the Br···HCCH and Cl···HCCH CCSD(T)/aug-cc-pVDZ calculations, one imaginary frequency was found (bold and marked *). This disappears in aug-cc-pVTZ calculations.

In the CCSD(T) calculations of both Br···HCCH and Cl···HCCH, only three of the four σ vibrations seen in the previous MP2 calculations were found. Instead a rocking vibration of the acetylene was found (bold and marked #). Therefore its position in the tables is out of formatting convenience rather than the vibrational mode being a linear stretching mode. This change in vibration modes is not seen in the I···HCCH complex most likely due to CCSD(T) calculations not being performed.

The second geometry is the “neutral T-shape” shown in Figures 34 to 36 with corresponding data in Tables 13 to 15. In this geometry, the halogen sits above the carbon triple bond.

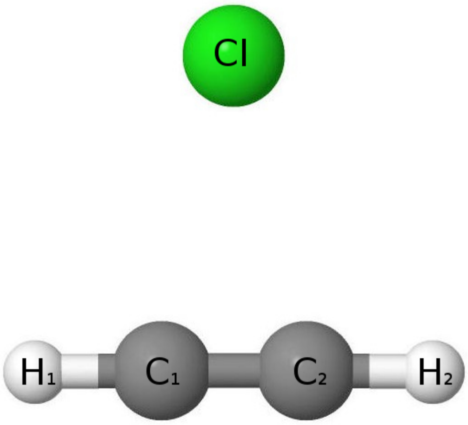

Figure 34. Schematic of the optimised geometry of Cl···HCCH neutral T-shape complex

Table 13. Calculated data of Cl···HCCH neutral T-shape complex at MP2/aug-cc-pVXZ and CCSD(T)/aug-cc-pVXZ (X = D, T). Values shown are the optimised geometry, vibration frequency wavenumbers with IR intensities in brackets (km mol^{-1}), zero point energies and final single point energies.

	MP2		**CCSD(T)**	
	pVDZ	**pVTZ**	**pVDZ**	**pVTZ**
r(Cl...HCCH)/Å	2.692	2.584	2.745	2.669
r(H-C)/Å	1.082	1.067	1.086	1.069
r(C-C)/Å	1.237	1.219	1.234	1.215
r(C-H)/Å	1.082	1.067	1.086	1.069
θ(C-C-H) / °	179.4	179.0	179.6	179.4
ω_1/cm^{-1}	3465 (1)	3493 (1)	3414 (1)	3461 (1)
ω_2/cm^{-1}	3365 (141)	3398 (138)	3317 (137)	3368 (133)
ω_3/cm^{-1}	1918 (29)	1930 (33)	1947 (23)	1967 (24)
ω_4/cm^{-1}	133 (16)	157 (20)	136 (13)	142 (15)
ω_5/cm^{-1}	1359 (<1)	931 (<1)	**75 (<1)$^{\#}$**	**96 (<1)$^{\#}$**
ω_6/cm^{-1}	728 (152)	764 (153)	719 (151)	759 (152)
ω_7/cm^{-1}	701 (106)	747 (103)	692 (107)	742 (104)
ω_8/cm^{-1}	500 (<1)	615 (<1)	542 (<1)	630 (<1)
ω_9/cm^{-1}	366 (<1)	404 (<1)	481 (<1)	606 (<1)
zpe /kcal.mol^{-1}	17.9	17.7	16.2	16.8
E_e /hartree	-536.674838	-536.807995	-536.722013	-536.864567
$E_{e/BSSE}$ /hartree	-536.670320	-536.801695	-536.718083	-536.858172
D_0 /cm^{-1}	6743	6489	6169	6156

$^{\#}$ change in vibrational mode from MP2 vibrational frequencies explained in detail later.

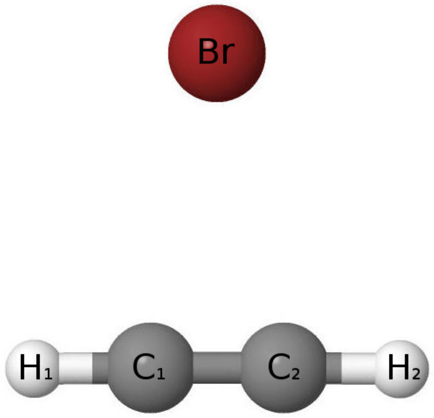

Figure 35. Schematic of the optimised geometry of Br···HCCH neutral T-shape complex

Table 14. Calculated data of Br···HCCH neutral T-shape complex at MP2/aug-cc-pVXZ and CCSD(T)/aug-cc-pVXZ (X = D, T). Values shown are the optimised geometry, vibration frequency wavenumbers with IR intensities in brackets (km mol^{-1}), zero point energies and final single point energies.

	MP2		**CCSD(T)**	
	pVDZ	**pVTZ**	**pVDZ**	**pVTZ**
r(Br...HCCH)/Å	2.933	2.853	2.971	2.919
r(H-C)/Å	1.082	1.069	1.086	1.069
r(C-C)/Å	1.236	1.217	1.234	1.214
r(C-H)/Å	1.082	1.067	1.086	1.069
θ(C-C-H) / °	179.5	179.2	179.7	179.5
ω_1/cm^{-1}	3465 (<1)	3497 (<1)	3414 (<1)	3462 (<1)
ω_2/cm^{-1}	3368 (136)	3375 (129)	3317 (134)	3368 (128)
ω_3/cm^{-1}	1928 (19)	1939 (19)	1953 (16)	1975 (15)
ω_4/cm^{-1}	104 (7)	110 (9)	117 (7)	97 (7)
ω_5/cm^{-1}	1144 (<1)	812 (<1)	**136 (<1)**[#]	**106 (<1)**[#]
ω_6/cm^{-1}	726 (151)	806 (149)	717 (150)	759 (151)
ω_7/cm^{-1}	703 (104)	799 (98)	694 (104)	744 (101)
ω_8/cm^{-1}	502 (0)	648 (0)	532 (<1)	627 (<1)
ω_9/cm^{-1}	296 (<1)	338 (<1)	484 (<1)	609 (<1)
zpe /kcal.mol^{-1}	17.5	17.6	16.2	16.8
E_e /hartree	-2649.551104	-2649.741313	-2649.595028	-2649.793659
$E_{e/BSSE}$ /hartree	-2649.547097	-2649.735964	-2649.591703	-2649.790250
D_0 /cm^{-1}	6593	6409	6196	6576

[#] change in vibrational mode from MP2 vibrational frequencies explained in detail later.

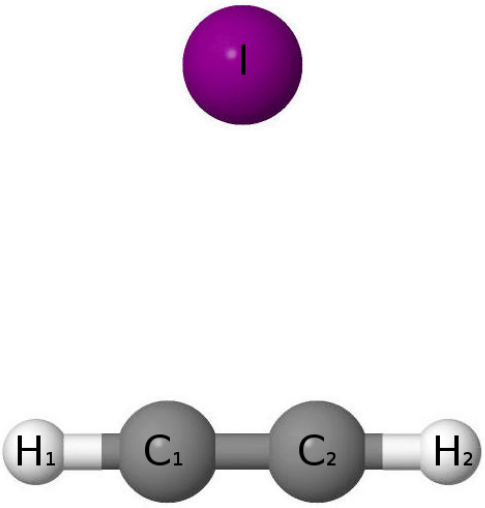

Figure 36. Schematic of the optimised geometry of I···HCCH neutral T-shape complex

Table 15. Calculated data of I···HCCH neutral T-shape complex at MP2/aug-cc-pVXZ (X = D, T). Values shown are the optimised geometry, vibration frequency wavenumbers with IR intensities in brackets (km mol^{-1}), zero point energies and final single point energies.

	MP2	
	pVDZ	**pVTZ**
r(I...HCCH)/Å	3.193	3.084
r(H-C)/Å	1.082	1.067
r(C-C)/Å	1.234	1.216
r(C-H)/Å	1.082	1.067
θ(C-C-H) / º	179.6	179.3
ω_1/cm^{-1}	3464 (<1)	3495 (<1)
ω_2/cm^{-1}	3379 (131)	3412 (129)
ω_3/cm^{-1}	1932 (10)	1949 (13)
ω_4/cm^{-1}	89 (4)	100.(5)
ω_5/cm^{-1}	875 (<1)	696 (<1)
ω_6/cm^{-1}	727 (151)	758 (154)
ω_7/cm^{-1}	705 (100)	751 (98)
ω_8/cm^{-1}	504 (<1)	618 (<1)
ω_9/cm^{-1}	322<1)	267 (<1)
zpe /kcal.mol^{-1}	17.2	17.2
E_e /hartree	-376.304652	-376.383122
$E_{e/BSSE}$ /hartree	-376.300918	-376.378394
D_0 /cm^{-1}	3039	3137

In all the optimised T-shape geometries the halogen moves progressively away from the acetylene as the halogen increases in mass and size. There is little distortion of the bond lengths of the acetylene. However, there is a breaking of the linearity of the acetylene as the C-H bonds are bent and the hydrogen atoms are bent away from the halogen. The interaction of the halogen on the bending of the hydrogen atoms is shown in the higher intensities of the degenerate vibrational modes ω_6 and ω_7.

The energies for all three complexes can be compared to their neutral-linear counterparts. In all cases the T-shape geometry is the lower energy hence it is more stable and favourable geometry. This could be due to the halogen sitting above the carbon triple bond. There is more electron density associated with the carbon triple bond compared to the C-H bonds. Therefore, the dispersion interaction between the acetylene and halogen is greater in the T-shape geometry.

Also seen in the Cl···HCCH and Br···HCCH calculations there is a change in a vibrational mode from MP2 to CCSD(T). The initial calculated mode ω_5 using MP2 is a free bending mode of all four atoms in the acetylene. When using CCSD(T) this vibrational mode disappears and instead a rocking motion of the acetylene is found (bolded and marked with $^{\#}$). Therefore the rocking vibration's position in the tables is due to formatting convenience. This change in the vibrational mode is not seen in the I···HCCH complex most likely due to CCSD(T) calculations not being performed.

For all complexes and geometries, the binding energy D_0 was calculated using the zero point energy and the BSSE corrected energy. The bromine and chlorine complexes display relatively similar values of binding energy across the three optimised geometries found with mostly similar patterns of changes in binding energy across the different sets of calculations. This likely demonstrates some influence of the basis sets and level of theory used on the results. In most cases the CCSD(T)/aug-cc-pVTZ results in the greatest binding energy value. The iodine-acetylene complexes demonstrate much lower values for the binding energies however, this is expected due to the use of ECP approximation in the calculations.

The calculated values for the anion complexes however, do not correspond with previous experimental data being almost double the above calculated values.[13] This suggests some problem with the calculations performed here and warrants repetition.

4.2 Bromide ECP calculation comparison

While ORCA supports optimisation of $Br^{-}\cdots HCCH$ at all levels of theory used here without ECP approximation, calculations were done at MP2/aug-cc-pVDZ PP and MP2/aug-cc-pVTZ PP of the three cluster geometries found previously. These results were then compared to the results found previously to see the effect of the ECP approximation (Tables 16 to 18).

Table 16. Comparison of optimised $Br^{-}\cdots HCCH$ data with and without ECP approximations at MP2/aug-cc-pVDZ and MP2/aug-cc-pVTZ. Values shown are the optimised geometry, vibration frequency wavenumbers with IR intensities in brackets (km mol^{-1}), zero point energies and final single point energies.

	No ECP approximation		**With ECP approximation**	
	pVDZ	**pVTZ**	**pVDZ PP**	**pVTZ PP**
r(Br...H_1)/Å	2.524	2.497	2.510	2.482
r(H_1-C_1)/Å	1.101	1.088	1.101	1.088
r(C_1-C_2)/Å	1.236	1.217	1.236	1.217
r(C_2-H_2)/Å	1.080	1.064	1.079	1.064
ω_1/cm^{-1} σ	3441 (6)	3477 (8)	3440 (6)	3477 (8)
ω_2/cm^{-1}	3140 (742)	3155 (721)	3136 (759)	3148 (737)
ω_3/cm^{-1}	1906 (118)	1923 (118)	1905 (122)	1922 (123)
ω_4/cm^{-1}	113 (11)	112 (11)	113 (11)	113 (11)
ω_5/cm^{-1} π	832 (61)	875 (51)	832 (59)	876 (50)
ω_6/cm^{-1}	531 (36)	619 (42)	532 (37)	619 (42)
ω_7/cm^{-1}	131 (<1)	133 (<1)	134 (<1)	133 (<1)
zpe /kcal.mol^{-1}	16.5	17.1	16.6	17.0
E_e /hartree	-2649.683486	-2649.875940	-497.013847	-497.163852

Table 17. Comparison of optimised Br···HCCH neutral linear data with and without ECP approximation at MP2/aug-cc-pVDZ and MP2/aug-cc-pVTZ. Values shown are the optimised geometry, vibration frequency wavenumbers with IR intensities in brackets (km mol^{-1}), zero point energies and final single point energies.

	No ECP approximation		**With ECP approximation**	
	pVDZ	**pVTZ**	**pVDZ PP**	**pVTZ PP**
r(Br...H)/Å	3.024	3.072	3.011	3.055
r(H-C)/Å	1.081	1.067	1.081	1.067
r(C-C)/Å	1.232	1.213	1.230	1.213
r(C-H)/Å	1.081	1.066	1.081	1.066
ω_1/cm^{-1} σ	3469 (2)	3502 (2)	3544 (3)	3504 (1)
ω_2/cm^{-1}	3375 (181)	3409 (169)	3378 (180)	3410 (170)
ω_3/cm^{-1}	1947 (2)	1965 (2)	2193 (2)	1968 (2)
ω_4/cm^{-1}	52 (<1)	45 (<1)	52 (<1)	45 (<1)
ω_5/cm^{-1} π	715 (103)	762 (101)	740 (103)	759 (100)
ω_6/cm^{-1}	712 (109)	758 (101)	735 (102)	759 (104)
ω_7/cm^{-1}	522 (1)	629 (1)	559 (1)	627 (1)
ω_8/cm^{-1}	520 (<1)	627 (1)	556 (1)	627 (1)
ω_9/cm^{-1}	58 (<1)	61 (<1)	103 (<1)	39 (<1)
ω_{10}/cm^{1}	43 (<1)	47 (<1)	94 (<1)	31
zpe /kcal.mol^{-1}	16.3	16.9	17.1	16.8
E_e /hartree	-2649.546630	-2649.736332	-496.878826	-497.025897

Table 18. Comparison of optimised Br···HCCH neutral T-shape data with and without ECP approximation at MP2/aug-cc-pVDZ and MP2/aug-cc-pVTZ. Values shown are the optimised geometry, vibration frequency wavenumbers with IR intensities in brackets (km mol^{-1}), zero point energies and final single point energies.

	No ECP approximation		**With ECP approximation**	
	pVDZ	**pVTZ**	**pVDZ PP**	**pVTZ PP**
r(Cl...HCCH)/Å	2.933	2.853	2.927	2.831
r(H-C)/Å	1.082	1.069	1.082	1.067
r(C-C)/Å	1.236	1.217	1.235	1.217
r(C-H)/Å	1.082	1.067	1.082	1.067
θ(C-C-H) / º	179.5	179.2	179.5	179.2
ω_1/cm^{-1}	3465 (<1)	3497 (<1)	3465 (<1)	3495.19 (<1)
ω_2/cm^{-1}	3368 (136)	3375 (129)	3364 (135)	3400.18 (132)
ω_3/cm^{-1}	1928 (19)	1939 (19)	1926 (16)	1941.65 (18)
ω_4/cm^{-1}	104 (7)	111 (9)	100 (<1)	114.04 (9)
ω_5/cm^{-1}	1144 (<1)	812 (<1)	1108 (<1)	793.23 (<1)
ω_6/cm^{-1}	726 (151)	805 (149)	726 (149)	763.20 (151)
ω_7/cm^{-1}	703 (104)	799 (98)	703 (104)	749.35 (101)
ω_8/cm^{-1}	502 (0)	648 (0)	502 (<1)	616.40 (<1)
ω_9/cm^{-1}	296 (<1)	338 (<1)	301 (<1)	339.93 (<1)
zpe /kcal.mol^{-1}	17.5	17.6	17.4	17.4
E_e /hartree	-2649.551104	-2649.741313	-496.883552	-497.031129

Across all three calculations the geometry and frequency wavenumber values remain very similar. The most significant difference seen is the large drop in single point energy when using ECP approximation. However this is expected due to the ECP approximation decreasing the number of electrons in the calculation. Therefore absolute values such as the single point energies cannot be compared between the two different calculations.

4.3 1D Potential energy scans

Relaxed one dimensional potential energy scans were performed on the Br$^-$···HCCH and Cl$^-$···HCCH complexes using MP2/aug-cc-pVDZ in Gaussian 09. These were done by first moving the halide around the acetylene, changing its geometry from linear to T-shape and allowing the geometry to optimise at each step, with just the angle fixed. The necessity of a relaxed scan is seen in the neutral angle scan where the distance between the acetylene and the halogen varies significantly depending on the geometry. It was found that when a fixed angle scan was performed on the neutral complex, the second minimum at the T-shape geometry was not found: the halogen was sitting out almost two Ångstroms further than the optimised geometry of the T-shape neutral. The opposite would have occurred scanning in the opposite direction: the halogen would have been much too close to the acetylene in the linear position.

In the following potential energy scans the angle is measured in reference to the plane of the acetylene as the halogen swings around the acetylene. Therefore, the linear geometry is observed at 0° and 180°. The T-shape geometry with the halogen sitting above the acetylene is observed at 90° and 270°.

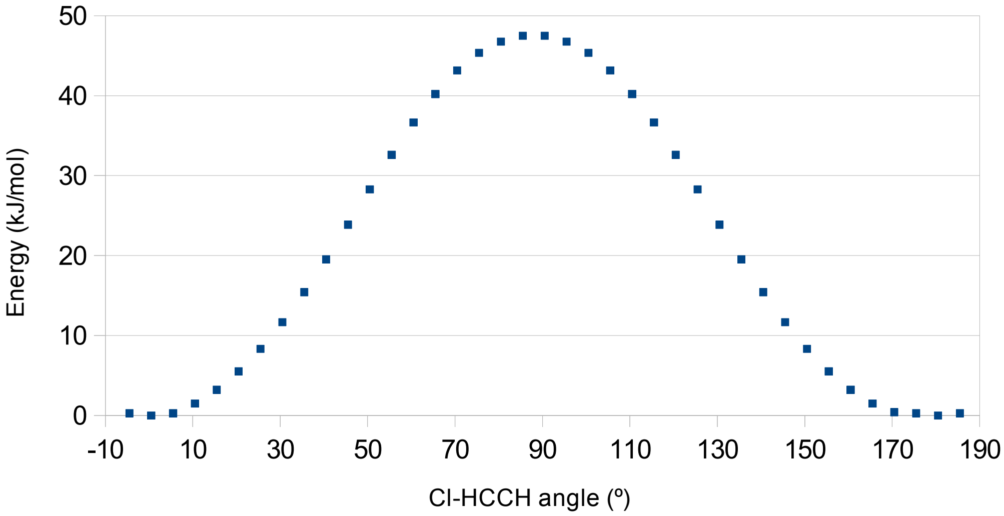

Figure 37. Relaxed potential energy scan of Cl$^-$···HCCH angle (anion).

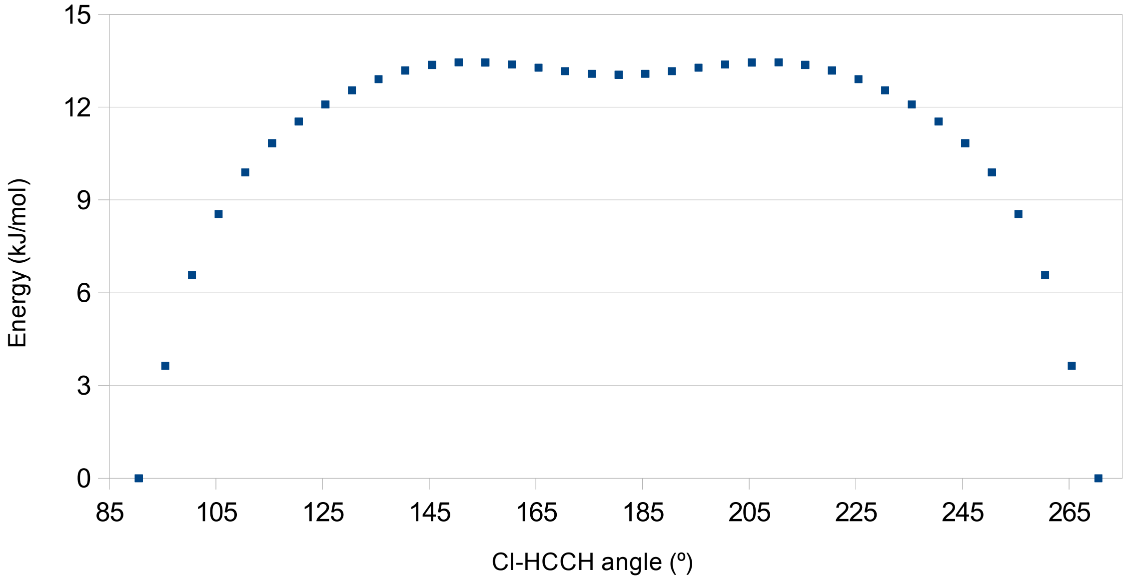

Figure 38. Relaxed potential energy scan of Cl···HCCH angle (neutral).

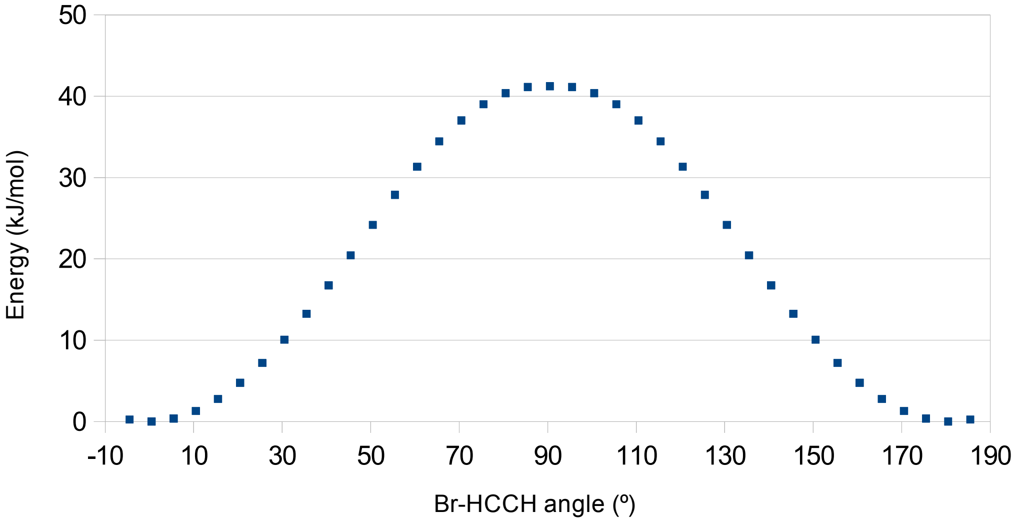

Figure 39. Relaxed potential energy scan of Br⁻···HCCH angle (anion).

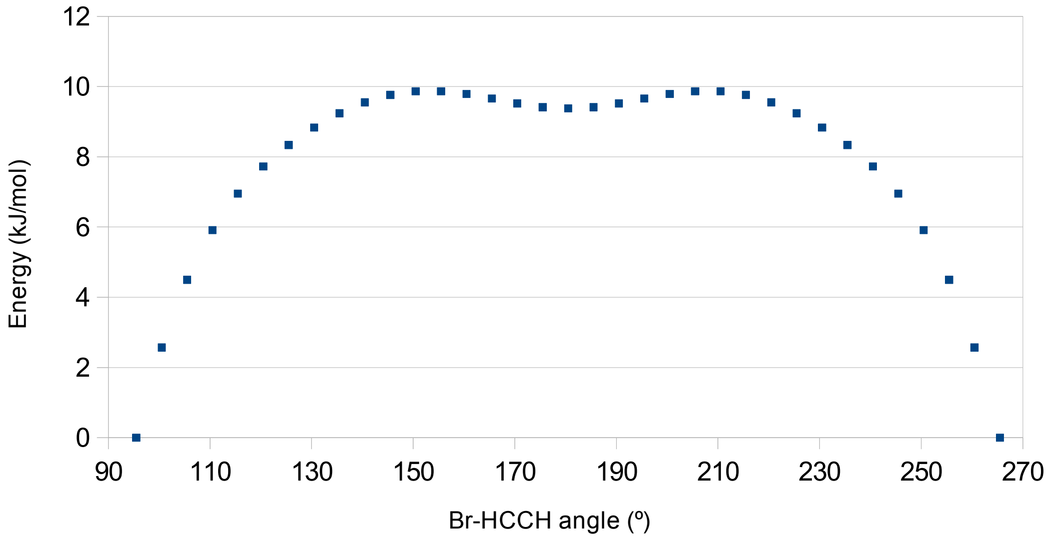

Figure 40. Relaxed potential energy scan of Br···HCCH angle (neutral)

As can be seen, both anion (Figure 37 and 39) and neutral (Figure 38 and 40) species for the two complexes have expected minima at the optimised geometries found. There are no additional minima. In the neutral species there is a much shallower minimum at the linear geometry, which corresponds to the lower energy found; i.e. the T-shape geometry is more stable and favourable than the linear geometry for the neutral complex. The lower energy at the minimum of the anion in comparison to the neutral species shows the increased stability that the anion-species has.

Using the known optimised geometries for the complexes, the second lot of 1D potential energy scans were performed by changing the bond length between the halide and the acetylene. The intermolecular distance refers to the distance between the halide and a dummy atom positioned in the centre of the acetylene molecule. For the neutral complexes, the bond scan was only done on the linear geometry due to time constraints.

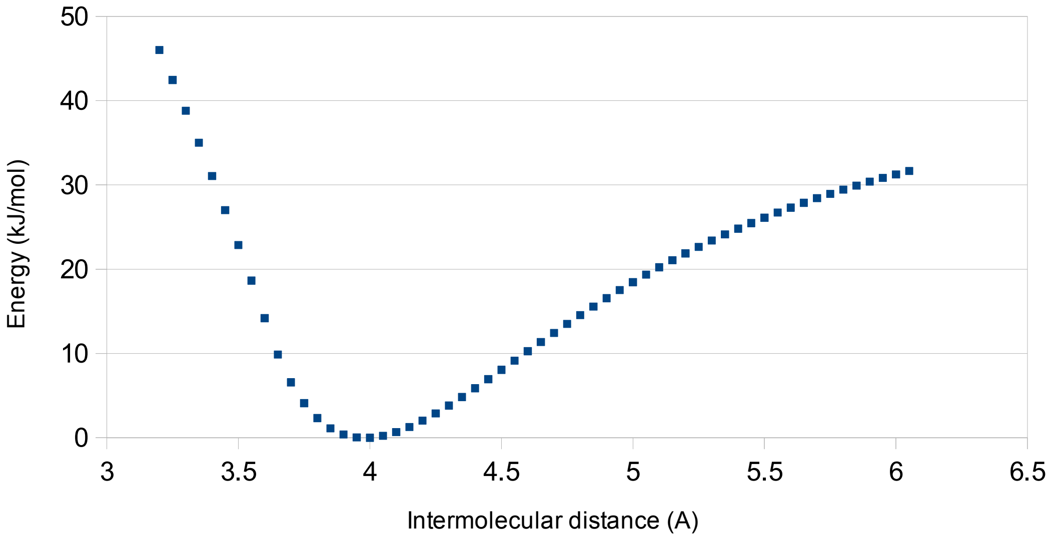

Figure 41. Relaxed potential energy scan of Cl^-···HCCH bond stretch (anion)

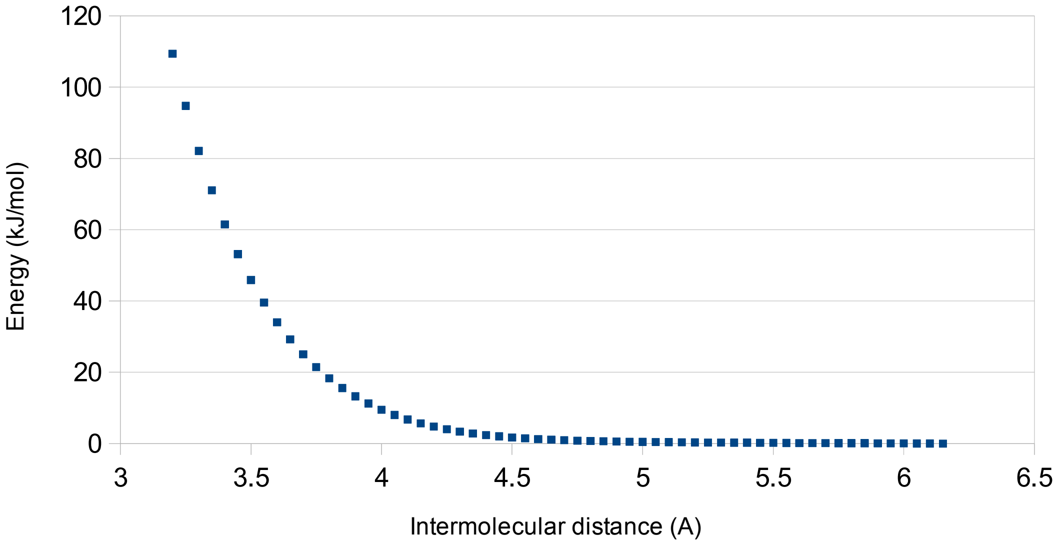

Figure 42. Relaxed potential energy scan of Cl···HCCH bond stretch (neutral)

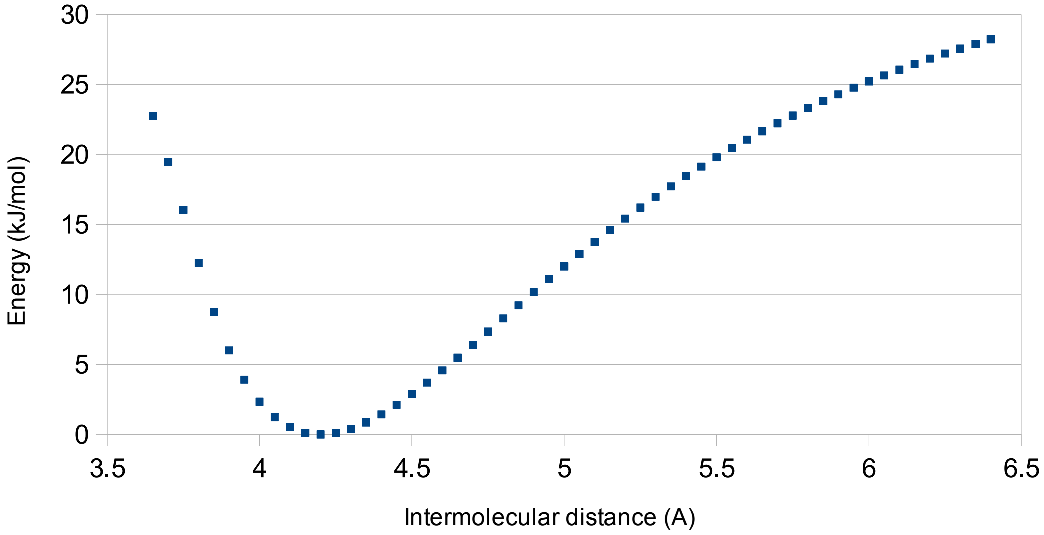

Figure 43. Relaxed potential energy scan of Br^{-}*···HCCH bond stretch (anion)*

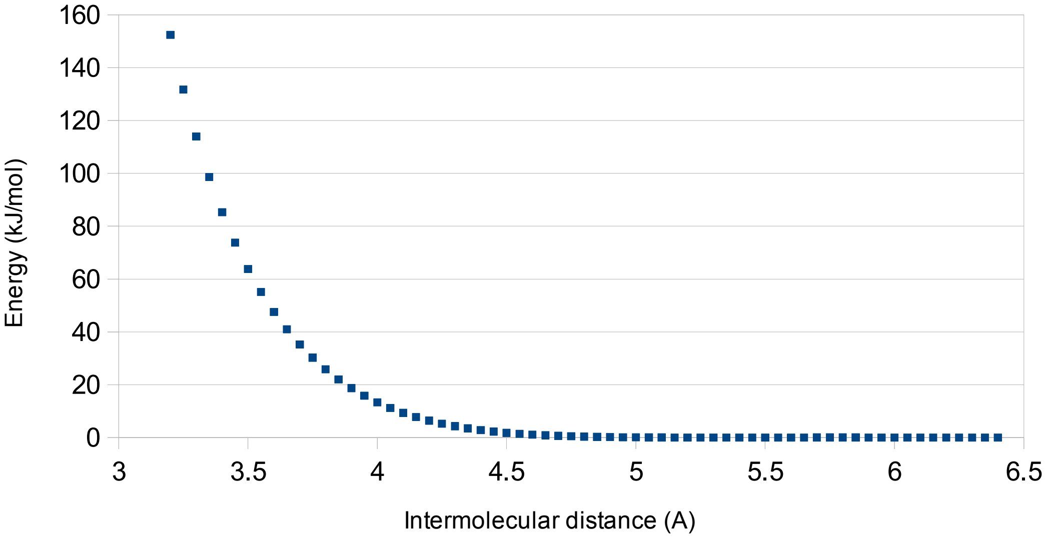

Figure 44. Relaxed potential energy scan of Br···HCCH bond stretch (neutral)

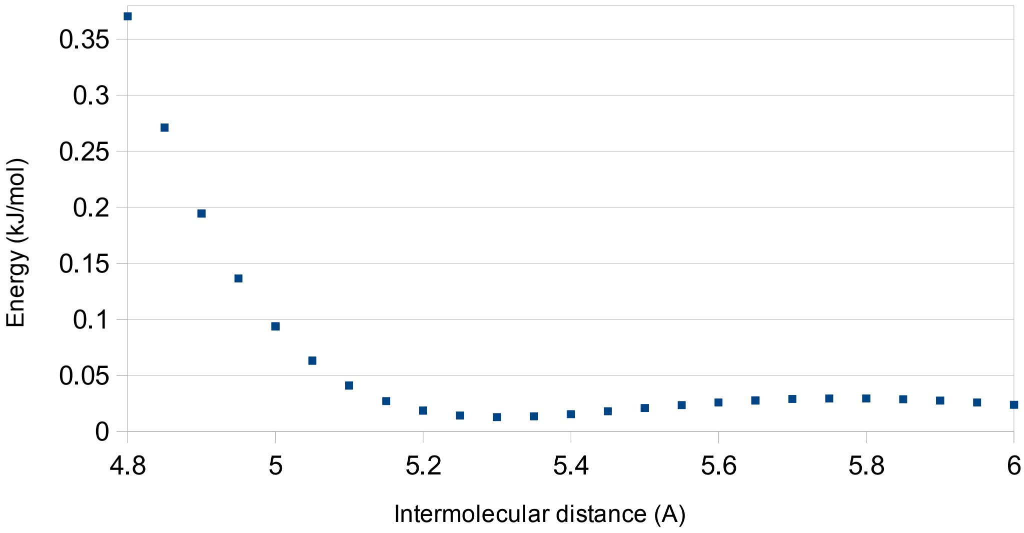

Figure 45. Zoomed in on the minimum of the relaxed potential energy scan of Br···HCCH bond stretch (neutral) (Figure 44)

In the bond scans of the anion species (Figure 41 and 43) both have a very clear and deep minimum at the bond length determined by the optimisation calculation. In contrast the Br···HCCH neutral linear bond scan (Figure 44) only has a very shallow minimum that is difficult to see without zooming in on the bottom of the curve (Figure 45). This shows an extremely weak interaction between the two units. However for the Cl···HCCH neutral species no minimum is seen (Figure 42). This is possibly due to not enough points being taken around that region or another scan at a higher level of theory being needed.

The difference in shape between the anion and neutral linear complexes show the change in stability caused by the change in intermolecular interaction caused by the loss of charge on the halogen. The neutral T-shape potential energy scan can possibly be predicted to have a more defined minimum than the linear neutral but, due to a similar decreased interaction between the acetylene and halogen, the minimum would not be as defined as seen in the anion bond length stretch scan.

4.4 NBO analysis

Natural Bond Orbital analysis has been performed on the Br···HCCH and Cl···HCCH species to further investigate the interaction between the halogen and the acetylene ligand. The NBO analyses were performed at MP2/aug-cc-pVDZ using Gaussian 09.

Table 19. Principal NBO analysis results of Cl···HCCH clusters

Type of complex	Donor	Acceptor	Stabilisation energy kcal/mol
Anion cluster	LP (4) Cl	BD* (1) H_1-C_1	15.13
Neutral linear cluster	LP (4) Cl	BD* (1) H_1-C_1	1.07
Neutral T-shape cluster	LP (4) Cl	BD* (1) H_1-C_1	0.05
	LP (4) Cl	BD* (1) C_2-H_2	0.05
	LP (4) Cl	BD* (2) C_1-C_2	0.21
	LP (4) Cl	BD* (3) C_1-C_2	1.41

Table 19 shows the NBO analysis results of the Cl···HCCH clusters revealing hydrogen bonding in the anion cluster by the transfer of electron density from the lone pair of the chloride to the anti-bonding orbital of H_1-C_1. This increase of electron density in the anti-bonding orbital of the H_1-C_1 bond correlates with the lengthening of the bond that was observed in the geometry optimisations.

The much weaker interaction between the chlorine and acetylene molecules in the linear neutral complex is also seen in the significantly lower transfer of electron density. The change in geometry from linear to T-shape has also changed the nature of the interaction between the acetylene and chlorine: the weak electron density transfer is seen mainly through the C-C triple bond.

The occupancy of the anti-bonding orbitals of the two C-H bonds in the acetylene in each of the cluster geometries is also compared to show the formation of bonds. These values are compared to the occupancies of bare acetylene and acetylene with a negative point charge in place of the anion.

Table 20. Comparison of occupancies of H-C bonds in Cl···HCCH clusters

	Occupancy of anti-bonding orbitals	
Type of complex	**H_1-C_1**	**H_2-C_2**
Bare acetylene	0.0052	0.0052
Anion cluster	0.0329	0.0060
Acetylene with negative point charge	0.0039	0.0061
Neutral linear cluster	0.0047	0.0026
Neutral T-shape cluster	0.0027	0.0027

The bare acetylene demonstrates an equal amount of electron density in both orbitals. In the anion cluster there is an increase in electron density in the H-C bond closest to the anion showing the formation of a H-bond with the chloride. This is also seen to a lesser degree in the neutral linear cluster. In comparison the polarisation of the acetylene by the negative point charge causes the electron density to be shifted to the bond away from the negative charge. The neutral T-shape has a similar occupancy ratio as the bare acetylene showing the lowering of the interaction between the H-C bonds and the chlorine.

The same analysis is shown with the Br···HCCH clusters in Tables 21 and 22.

Table 21. Principal NBO analysis results of Br···HCCH clusters

Type of complex	**Donor**	**Acceptor**	**Stabilisation energy kcal/mol**
Anion cluster	LP (4) Br	BD* (1) H_1-C_1	12.71
Neutral linear cluster	LP (4) Br	BD* (1) H_1-C_1	1.09
Neutral T-shape cluster	LP (3) Br LP (3) Br LP (3) Br LP (3) Br	BD* (1) H_1-C_1 BD* (1) C_2-H_2 BD* (2) C_1-C_2 BD* (3) C_1-C_2	0.04 0.04 1.43 0.06

Table 22. Comparison of occupancies of H-C bonds Br···HCCH clusters

	Occupancy of anti-bonding orbitals	
Type of complex	**H_1-C_1**	**H_2-C_2**
Bare acetylene	0.0052	0.0052
Anion cluster	0.0309	0.0061
Acetylene with negative point charge	0.0040	0.0060
Neutral linear cluster	0.0049	0.0026
Neutral T-shape cluster	0.0026	0.0026

The Br···HCCH clusters demonstrate a similar trend to the Cl···HCCH clusters regarding the transfer of electron density for all types of clusters investigated. The largest difference between the two halides and their interaction with acetylene is seen in the stabilisation energy of the anion clusters. Bromide-acetylene is lower, which agrees with previous research that bromide has weaker proton accepting ability and thus forms a weaker bond with acetylene.

Unfortunately, due to issues encountered during the I···HCCH calculations, NBO analysis on the I···HCCH clusters could not be completed. From what has been observed in previous calculations however, it can be expected that the iodide-acetylene NBO analysis will follow a similar trend as seen in the chloride- and bromide-acetylene results: a lower stabilisation energy and a similar movement of electron density into anti-bonding orbitals across the different types of complexes.

5. Future work

Despite the experimental problems faced this year, the work done has set the foundations for further study of this group of halide-acetylene clusters.

Upon the TOF-PES working again, photoelectron spectra of the three clusters should be taken. While the current gas mixture method creates a workable mixture, some work is still needed in order to further optimise the gas mixture ratios. There have been suggested changes to the gas mixing station in order to improve diffusion rates such as implementing pulsing nozzles similar to the one currently used for the gas mixture inside the TOF-PES to alternate between addition of argon and acetylene. Also suggested was having a removable gas mixing station to manually agitate the gas mixture.

Also awaiting the revival of the TOF-PES is the testing of the new permanent magnets. Their implementation should hopefully see improved photoelectron spectra.

One main issue seen in this work is the abundance of the secondary series of clusters in the mass spectra. Further experimentation with the gas mixing ratios should be done to try and minimise these clusters being formed. This would allow larger clusters of the halide-acetylene to be explored and thus begin looking at the solvation shell formation around the halides with acetylene. This should also be aided with the addition of the piezo nozzle later which will hopefully aid in producing larger clusters in greater amounts and provide needed stability and reliability in the nozzle for the TOF-PES.

Further calculations need to be performed: the missing 1D potential energy scans and 2D and 3D scans. The CCSD(T) calculations of the three I···HCCH complexes still need to be done. The changes in the vibrational frequency results seen in the neutral complexes going from MP2 to CCSD(T) and the much larger than expected calculated values of the binding energies for the complexes warrants further exploration.

6. Conclusion

While the TOF-PES experienced multiple issues throughout the year, mass spectra were successfully taken for all three series of clusters $Cl^{-}\cdots(HCCH)_n$, $Br^{-}\cdots(HCCH)_n$ and $I^{-}\cdots(HCCH)_n$. All three mass spectra showed amounts of larger clusters being made. However, due to a high amount of additional species being present in the gas mixtures, clusters exceeding the first solvation shell size were not able to be seen. Preliminary photoelectron spectra were able to be taken that showed the expected shift in binding energy with the addition of ligands, with further work into the photoelectron spectra of these complexes to be done upon the TOF-PES being back in working condition.

Ab initio calculations were performed on all three anion clusters and these calculations expanded on previous work to also investigate the neutral species. It was found the T-shape is the favoured neutral geometry for all three species. NBO analysis provided an insight into the shift in electron density that helped explain the observed changes and trends in geometry across the different complexes. It also further confirmed stronger bonding of the anion complexes in comparison to the neutral complexes.

7. References

(1) Bieske, E.J.; *Chem. Soc. Rev*. **2003**, *32,* 231–237.

(2) Wild, D.A.; Bieske, E.J.; *International Reviews in Physical Chemistry.* **2003**, *22,* 129–151.

(3) Arnold, D.W.; Bradforth, S.E.; Kim, E.H.; Neumark, D.M.; *J. Chem. Phys*. **1995**, *102*, 3510-3518.

(4) Kovacs, A.; Varga, Z.; *Coord. Chem. Rev.* **2006**, *250,* 710–27.

(5) Courtesy of Lapere, K.M.

(6) Lapere, K. University of Western Australia, (Honours Thesis). **2009**.

(7) Dale, S. University of Western Australia, (Honours Thesis). **2012**.

(8) Boesl, U.; Knott, W.J.; *Mass Spctrom. Rev.* **1998**, *17*, 275-305.

(9) Lapere, K.M.; LaMacchia. R.J.; Quak, L.H.; McKinley, A.J.; Wild, D.A.; *Chem. Phys. Lett.* **2011**, *504,* 13–9.

(10) Weiser, P.S.; Wild, D.A.; Bieske, E.J.; *Chem. Phys. Lett.* **1999**, *299*, 303–308.

(11) Wild, D.A.; Milley, P.J.; Loh, Z.M.; Weiser, P.S.; Bieske, E.J.; *Chem. Phys. Lett.* **2000**, *323*, 49–54.

(12) Weiser, P.S.; Wild, D.A.; Bieske, E.J.; *J. Chem. Phys*. **1999**, *110*, 9443–9449.

(13) Botschwina, P.; Oswald, R.; *J. Chem. Phys.* **2002**, *117*, 4800-4802

(14) Botschwina, P.; Stoll, H.; *Phys. Chem. Chem. Phys.* **2001**, *3*, 1965-1972

(15) Botschwina, P.; Dutoi, T.; Mladenovic, M.; Oswald, R.; Schmatz, S.; Stoll, H.; *Faraday Discuss*. **2001**, *118*, 433-453

(16) Quak, H. University of Western Australia, (Honours Thesis). **2009**.

(17) Wild, D.A.; Loh, Z.M.; Bieske, E.J.; *Aust. J. Chem.* **2011**, *64,* 633–637.

(18) Wild, D.A.; Milley, P.J.; Loh, Z.M.; Wolynec, P.P.; Weiser, P.S.; Bieske, E.J.; *J. Chem. Phys*. **2000**, *113,* 1075–1080.

(19) Wiley, W.C.; McLaren, I.H.. *Rev Sci. Instrum.* **1955**, *26*, 1150-1157.

(20) Courtesy of Wild, D.A.

(21) Wild, D.A.; Loh, Z.M.; Wilson, R.L.; Bieske, EJ. *Chem. Phys. Lett.* **2003**, *369*, 684–690.

(22) LaMacchia, R. University of Western Australia, (Honours Thesis). **2008**.

(23) Cheshnovsky, O.; Yang, S.H.; Pettiette, C.L.; Craycraft, M.J.; Smalley, R.E. *Rev. Sci. Instrum.* **1987**, *58*, 2131-2137.

(24) Neese, F. *ORCA,* University of Bonn: Germany, 2007

(25) Frisch, M. J.; Trucks, G. W.; Schlegel, H. B.; Scuseria, G. E.; Robb, M. A.; Cheeseman, J. R.; Scalmani, G.; Barone, V.; Mennucci, B.; Petersson, G. A.; Nakatsuji, H.; Caricato, M.; Li, X.; Hratchian, H. P.; Izmaylov, A. F.; Bloino, J.; Zheng, G.; Sonnenberg, J. L.; Hada, M.; Ehara, M.; Toyota, K.; Fukuda, R.; Hasegawa, J.; Ishida, M.; Nakajima, T.; Honda, Y.; Kitao, O.; Nakai, H.; Vreven, T.; Montgomery, J. A., Jr.; Peralta, J. E.; Ogliaro, F.; Bearpark, M.; Heyd, J. J.; Brothers, E.; Kudin, K. N.; Staroverov, V. N.; Kobayashi, R.; Normand, J.; Raghavachari, K.; Rendell, A.; Burant, J. C.; Iyengar, S. S.; Tomasi, J.; Cossi, M.; Rega, N.; Millam, N. J.; Klene, M.; Knox, J. E.; Cross, J. B.; Bakken, V.; Adamo, C.; Jaramillo, J.; Gomperts, R.; Stratmann, R. E.; Yazyev, O.; Austin, A. J.; Cammi, R.; Pomelli, C.; Ochterski, J. W.; Martin, R. L.; Morokuma, K.; Zakrzewski, V. G.; Voth, G. A.; Salvador, P.; Dannenberg, J. J.; Dapprich, S.; Daniels, A. D.; Farkas, Ö.; Foresman, J. B.; Ortiz, J. V.; Cioslowski, J.; Fox, D. J. *Gaussian 09*, Gaussian, Inc.: Wallingford CT, 2009.

(26) Møller, C.; Plesset, M. S.; *Phys. Rev.* **1934**, *46*, 618-622.

(27) Raghavachari, K.; G. W. Trucks, J. A. Pople, and M. Head-Gordon, *Chem. Phys. Lett.* **1989**, *157*, 479-483.

(28) Dunning, Jr.; T. H.; *J. Chem. Phys.* **1989**, *90*, 1007-1023.

(29) Kendall, R. A.; Dunning, Jr., T. H.; Harrison, R. J. *J. Chem. Phys.* **1992**, *96*, 6796-6806.

(30) Woon, D. E.; Dunning, Jr., T. H., *J. Chem. Phys.* **1993**, *98*, 1358-1371

(31) Wilson, A.K.; Woon, D.E.; Peterson, K.A.; Dunning, Jr., T.H. *J. Chem. Phys.* **1999**, *110*, 7667-7676

(32) Glendening, E. D.; Badenhoop, J. K.; Reed, A. E.; Carpenter, J. E.; Bohmann, J. A.; Morales, C. M.; Weinhold, F. *NBO 5.0*, Theoretical Chemistry Institute, University of Wisconsin, Madison WI, 2001